

Changes in northern hemisphere temperature variability shaped by regional warming patterns

Article

Accepted Version

Tamarin-Brodsky, T., Hodges, K. ORCID: <https://orcid.org/0000-0003-0894-229X>, Hoskins, B. J. and Shepherd, T. G. ORCID: <https://orcid.org/0000-0002-6631-9968> (2020) Changes in northern hemisphere temperature variability shaped by regional warming patterns. *Nature Geoscience*, 13. pp. 414-421. ISSN 1752-0894 doi: <https://doi.org/10.1038/s41561-020-0576-3> Available at <https://centaur.reading.ac.uk/89972/>

It is advisable to refer to the publisher's version if you intend to cite from the work. See [Guidance on citing](#).

To link to this article DOI: <http://dx.doi.org/10.1038/s41561-020-0576-3>

Publisher: Nature Publishing Group

All outputs in CentAUR are protected by Intellectual Property Rights law, including copyright law. Copyright and IPR is retained by the creators or other copyright holders. Terms and conditions for use of this material are defined in the [End User Agreement](#).

www.reading.ac.uk/centaur

CentAUR

Central Archive at the University of Reading

Reading's research outputs online

Changes in northern hemisphere temperature variability shaped by regional warming patterns

Talia Tamarin-Brodsky¹, Kevin Hodges^{1,2}, Brian J. Hoskins¹, and Theodore G. Shepherd¹

¹*Department of Meteorology, University of Reading, Reading, United Kingdom*

²*National Centre for Atmospheric Science, University of Reading, Reading, UK*

Global warming involves changes not only in the mean atmospheric temperature, but also in its variability and extremes. Here we use a feature-tracking technique to investigate the dynamical contribution to temperature anomalies in the northern hemisphere in CMIP5 climate-change simulations. We develop a simple theory to explain how temperature variance and skewness changes are generated dynamically from mean temperature gradient changes, and demonstrate the crucial role of regional warming patterns in shaping the distinct response of cold and warm anomalies. We also show that skewness changes must be taken into account, in addition to variance changes, in order to correctly capture the projected temperature variability response. These changes in variability may impact humans, agriculture and animals, as they experience not only a warmer mean climate, but also a new likelihood of temperature anomalies within that climate.

Atmospheric temperature is often described as the mean temperature and its variance (Fig. 1), the latter measuring the strength of fluctuations around the average temperature. Assuming a Gaussian distribution of the underlying Probability Density Function (PDF), the mean and variance capture the essence of the observed temperature variability¹⁻³. However, there is increasing evidence

21 that temperature PDFs are characterized by nonzero skewness, which implies a non-Gaussian tem-
22 perature distribution⁴⁻¹². Skewness, defined as $S = \overline{T'^3} / (\overline{T'^2})^{\frac{3}{2}}$ (where bar signifies a seasonally-
23 varying time average and T' denotes the temperature anomalies) measures the asymmetry between
24 the positive and negative tails of the PDF, and is positive in regions where large warm anomalies
25 are more frequent, and negative in regions where large cold anomalies are more frequent. There-
26 fore, the spatial structure of skewness (Fig. 2) has important implications for regional climate and
27 weather^{5, 7, 9, 13-19}.

28 Under global warming, the spatial distribution of the mean temperature and its variability
29 are projected to change, leading to significant climate impacts^{20,21}. Many studies have exam-
30 ined the mean temperature response as well as its variance and extremes using climate change
31 simulations^{1,3,5,8,15,18,22-24}. Although several studies have highlighted the importance of studying
32 the response of temperature skewness to climate change^{6,10,11,13,15,18,21,25-29}, changes in extreme
33 cold and warm temperature events are still typically attributed to changes in the mean and variance
34 alone (e.g., Figure 1.8 in the 5th IPCC report³⁰). Here we take a dynamical approach to study tem-
35 perature variability in the Northern Hemisphere (NH), employing a Lagrangian feature-tracking
36 algorithm to identify and track temperature anomalies. This allows us to directly evaluate the
37 separate changes in the intensity of cold and warm anomalies.

38 To concentrate on the dynamical origin of the temperature changes, we examine the 850hPa
39 level rather than the surface anomalies. The 850hPa level is a widely-used near-surface level^{3,10,24}
40 as it is typically above the boundary layer, but still highly correlated with the surface during strong

41 cold and warm temperature events (Extended Data Fig. 1). The relation to surface temperature
42 changes is discussed in the final section.

43 **Projected temperature changes**

44 We first present the Eulerian temperature variability changes for winter (DJF) and summer (JJA),
45 for the ensemble-averaged CMIP5 response for the mean temperature, variance and skewness
46 (see Methods). The 850 hPa wintertime mean temperature exhibits an excess warming in the
47 high-latitude NH (Fig. 1c), implying a weakening of the meridional (north-south) temperature
48 gradient^{3,22,24} (Extended Data Fig. 4). In addition, the relatively colder continental land masses
49 warm more rapidly than the oceans, so the zonal (east-west) temperature gradients also decrease
50 over most of the NH. To first order, the general decrease of the temperature gradients in winter
51 leads to a decrease in the temperature variance, since by advection arguments a weaker gradient
52 implies weaker anomalies^{3,22,24}. However, some regions such as the Mediterranean and the Iberian
53 Peninsula exhibit a slight variance increase (Fig. 1d). In summer, the already warmer continents
54 warm more rapidly than the oceans (Fig. 1g), such that the zonal temperature gradients increase²⁴
55 (Extended Data Fig. 4). There is less agreement between the models regarding the sign of the
56 variance change in summer, but a robust increase in variance is projected over central Europe^{5,31}
57 (Fig. 1h).

58 The temperature skewness changes provide further important information. For example, the
59 generally positive skewness change over most of the NH during winter (Fig. 2c) implies, together

60 with the variance decrease, that it is the cold anomalies that weaken the most. In summer, the in-
61 crease in variance over central Europe is accompanied by a negative skewness change in the south-
62 ern regions, and a slight positive skewness change in the northeastern regions (Fig. 2g). Hence,
63 it is mainly the cold anomalies that intensify in southern Europe, and mainly the warm anomalies
64 that intensify in northeastern Europe.

65 **Lagrangian temperature variability**

66 Lagrangian feature-tracking is a commonly-applied technique in the field of stormtracks, used
67 for studying cyclones and anticyclones³², but is applied here for temperature anomalies instead.
68 The approach was recently used by the authors to study temperature variability and its projected
69 changes in the Southern Hemisphere (SH)²⁸. In the SH, the temperature skewness is characterized
70 by a band of positive skewness on the poleward side of the midlatitude storm tracks, and a band
71 of negative skewness on the equatorward side. In the NH, the existence of large continents com-
72 plicates this picture, and high spatial heterogeneity in skewness is observed rather than a simple
73 dipole structure.

74 The feature-tracking algorithm is applied separately for the 850 hPa cold and warm tem-
75 perature anomalies, and the spatial distribution of their mean intensities then constructed (Fig. 3).
76 This allows the temperature variance to be decomposed into the separate contributions from cold
77 (Fig. 3a,e) and warm anomalies (Fig. 3b,f). While the intensity (in absolute value) of both types
78 of anomalies generally maximizes over continents, notable differences are observed, with some

79 regions experiencing stronger cold anomalies and others stronger warm anomalies.

80 The decomposition into cold and warm temperature anomalies allows us to directly evaluate
81 the distinct contribution of each to the projected regional changes. For example, the projected
82 winter changes in the mean intensity of cold (Fig. 3c) and warm (Fig. 3d) anomalies clearly show
83 that while both types of anomalies are projected to decrease in magnitude, the cold anomalies
84 weaken more. In addition, a limited strengthening of both is found over some regions in central and
85 southern Europe (although less model agreement is found there). In summer, the projected changes
86 in the intensity of both cold and warm anomalies show robust increases over central Europe, with
87 cold anomalies increasing to the northwest and extending towards the British Isles and the Atlantic
88 Ocean, and warm anomalies increasing mainly in the northeastern parts.

89 Assuming small asymmetry between the cold and warm anomalies, their mean intensities
90 can be used to estimate the temperature variance and skewness as

$$\sigma^2 \approx \left(\frac{1}{2}(T_w + T_c) \right)^2, \quad (1)$$

and

$$S \approx \frac{T_w - T_c}{\frac{1}{2}(T_w + T_c)} \quad (2)$$

91 (see section 2 in the Supplementary Information for the derivation of this approximation), where
92 $T_c = |T'_c|$ and $T_w = |T'_w|$ denote the average absolute intensity of the cold and warm temperature
93 anomalies, respectively. The approximate variance (1) measures the power of the average intensity,

94 while the approximate skewness (2) measures the normalized asymmetry between the cold and the
95 warm anomalies (and equals zero if $T_c = T_w$). The approximate skewness, estimated using the
96 tracking statistics of the mean intensities, recovers well the temperature skewness (Fig. 2b,f) and
97 its projected changes (Fig. 2d,h), albeit with somewhat smaller values.

98 The dynamical origin of the changes in cold and warm temperature anomalies is demon-
99 strated next for two regional examples, and then generalized using a simple model.

100 **Regional examples**

101 We first examine a region in east-central North America (black box in Fig. 1-3, panels a-d), for
102 which the ensemble-mean historical temperature PDF is negatively skewed in winter (Fig. 4a, solid
103 line). The tracking results indeed show that the intensities of cold anomalies that pass through this
104 region in the historical simulations (Fig. 4b, blue solid lines) reach larger magnitudes than the warm
105 anomalies (Fig. 4c, red solid lines) (see Methods). The projected temperature variability changes
106 in this region are representative of the changes over most of the NH during winter, and exhibit a
107 decrease in variance and a positive skewness change (Fig. 4a, dashed line). Consistent with this,
108 both the cold and warm anomalies that cross the region weaken in the projected simulations (blue
109 and red dashed lines in Figs. 4b and 4c, respectively), but the cold anomalies weaken substantially
110 more such that there is a positive skewness change. There is also a robust agreement between
111 models regarding the sign of these projected changes (Fig. 4d-g).

112 A composite analysis of strong cold and warm anomalies that pass through the region (see

113 Methods) provides further insight regarding the dynamical origin of these changes. Figs. 4h
114 and 4i show the projected anomalous circulation associated with strong cold and warm events,
115 respectively, overlaid with the projected background temperature change. For strong cold events
116 (Fig. 4h), the anomalous northerly flow entering the region experiences a warmer background tem-
117 perature to the north, hence the air is advected over a region with reduced meridional temperature
118 gradient (Extended Data Fig. 4), and the cold anomalies weaken. A smaller decrease occurs for
119 the anomalous southerly flow entering the region during the warm events (Fig. 4i), resulting in a
120 smaller reduction of the warm anomalies.

121 Without considering the skewness changes, one overestimates the risk ratio (calculated as
122 the ratio of the Cumulative Density Functions between historical and projected temperatures) of
123 low temperature extremes (dashed blue line in Fig. 4j), and underestimates the risk ratio of high
124 temperature extremes (dashed red line in Fig. 4k). For example, in this region, the risk ratio of
125 reaching a temperature below 250K is doubled (from 0.06 to 0.12) (Fig. 4j), while the risk ratio
126 of exceeding a temperature of 285K is underestimated by about 60% (from 3.9 to 1.6) (Fig. 4k), if
127 skewness changes are neglected. Repeating this analysis for kurtosis shows much smaller changes
128 (Extended Data Fig. 5).

129 Over central Europe during summer (black box in Fig. 1-3, panels e-h), the ensemble mean
130 historical temperature PDF is positively skewed (Fig. 5a, solid line). Variance increases while
131 skewness slightly decreases in the projected simulations (Figs. 5a-g), although there is greater
132 model spread in the sign of the projected skewness change (Figs. 5g). The projected background

133 temperature increase is maximized around southern Europe and the northern Mediterranean re-
134 gion, and the meridional temperature gradient therefore increases over central Europe (Extended
135 Data Fig. 4). Hence, during strong cold events, the northwesterly flow entering the region (Fig. 5h)
136 experiences a stronger background temperature gradient, and the cold anomalies intensify. Simi-
137 larly, during strong warm events, the anomalous southerly flow entering central Europe (Fig. 5i)
138 experiences a stronger meridional temperature gradient, albeit somewhat smaller, and the warm
139 temperature anomalies therefore also intensify, but to a lesser extent. Note that the increase in
140 the zonal temperature gradient over central Europe and the west of Iberia (Extended Data Fig. 4)
141 also contributes to the intensification of the warm anomalies. Overall, the skewness changes are
142 relatively small and slightly negative when averaged over central Europe (Fig. 5g).

143 Neglecting the skewness changes nevertheless results in an underestimation of the extreme
144 cold tail (dashed blue line in Fig. 5j) and an overestimation of the extreme warm tail (dashed red
145 line in Fig. 5k). For example, in this region the risk ratio of reaching a temperature below 275K
146 is almost halved (from 0.06 to 0.03) if one neglects the skewness changes (Fig. 5j), while the
147 risk ratio of exceeding a temperature above 304K is overestimated by about 20% (from 42 to 50)
148 (Fig. 5k).

149 **Dynamical origin of temperature changes**

150 The two regional examples discussed above can be generalized using simple arguments. Given that
151 strong cold and warm temperature anomalies are mostly associated with northerly and southerly

152 winds, respectively²², we can understand the first-order changes in variance and skewness given
 153 the changes in the meridional background temperature gradients as follows. From Taylor's theo-
 154 rem, one can express the cold and warm temperature anomalies arising from horizontal advection
 155 as $T'_c = -\eta_N \bar{T}_{Ny}$ and $T'_w = -\eta_S \bar{T}_{Sy}$, respectively. Here, $\eta_N < 0$ is the meridional displacement
 156 of the cold anomaly (which is negative since it is coming from the north), and $\eta_S > 0$ is the merid-
 157 ional displacement of the warm anomaly (coming from the south). We further denote \bar{T}_{Ny} as the
 158 averaged background temperature gradient experienced by the cold anomaly during its movement
 159 from the north, and similarly \bar{T}_{Sy} for the warm anomaly.

160 It is clear from the expressions above for T'_c and T'_w and (2) for the approximate skewness
 161 how a nonzero local temperature skewness can be obtained, $S \approx \frac{|\eta_S \bar{T}_{Sy}| - |\eta_N \bar{T}_{Ny}|}{\frac{1}{2}(|\eta_S \bar{T}_{Sy}| + |\eta_N \bar{T}_{Ny}|)}$, if $|\eta_N \bar{T}_{Ny}| \neq$
 162 $|\eta_S \bar{T}_{Sy}|$. Moreover, if nonuniform changes in the background temperature gradient occur, both
 163 the variance and skewness can change locally. Denoting $\Delta \bar{T}_{Ny}$ and $\Delta \bar{T}_{Sy}$ as the changes in the
 164 meridional background temperature gradient to the north and south of a region, one finds $\Delta T'_c =$
 165 $-\eta_N \Delta \bar{T}_{Ny}$ for the cold anomalies, and $\Delta T'_w = -\eta_S \Delta \bar{T}_{Sy}$ for the warm anomalies. Here we have
 166 assumed for simplicity that η_N and η_S remain the same in the future climate, but the meridional
 167 displacements can generally change too (although in the regions we have examined, the changes
 168 appear to be small, Extended Data Fig. 6). In the limit of small asymmetry, using (1) and (2) for the
 169 approximate variance and skewness (respectively) and the expressions above, we find (see section
 170 3 in the Supplementary Information):

$$\Delta\sigma^2 \approx \sigma^2 \left[\frac{\Delta\bar{T}_{S_y}}{\bar{T}_{S_y}} + \frac{\Delta\bar{T}_{N_y}}{\bar{T}_{N_y}} \right], \quad (3)$$

171 and

$$\Delta S \approx \frac{\Delta\bar{T}_{S_y}}{\bar{T}_{S_y}} - \frac{\Delta\bar{T}_{N_y}}{\bar{T}_{N_y}}. \quad (4)$$

172 Hence, depending on the sign and magnitude of the relative temperature gradient changes to
 173 the north and to the south, the variance and skewness can either increase or decrease. Note that
 174 close to localized temperature gradients (e.g., due to orography or ocean-continent boundaries),
 175 zonal gradients also can be significant in influencing the temperature variability³³. The equations
 176 above can be easily generalized to include zonal gradients by calculating the derivatives in the
 177 direction of largest gradient, which will have a westerly/easterly component in these regions.

178 If the gradient changes both oppose the original temperature gradients (i.e., $\frac{\Delta\bar{T}_{N_y}}{\bar{T}_{N_y}} < 0$ and
 179 $\frac{\Delta\bar{T}_{S_y}}{\bar{T}_{S_y}} < 0$), as is the case for most of the NH during winter, and for the first region examined above,
 180 then (3) predicts a negative variance change. Furthermore, if the relative decrease to the north $\frac{\Delta\bar{T}_{N_y}}{\bar{T}_{N_y}}$
 181 is larger than the relative decrease to the south $\frac{\Delta\bar{T}_{S_y}}{\bar{T}_{S_y}}$, then (4) predicts a positive skewness change.
 182 The actual changes are captured nicely by the simplified equations for east-central North America
 183 during winter, as presented in Figs. 6a and 6b, which show the predicted vs. actual variance and
 184 skewness changes, respectively, across the CMIP5 models. For almost all of the models, the sign
 185 of the variance change agrees with the background temperature gradient decrease (Fig. 6a). The
 186 theory also helps understand some of the model spread, as models that predict a larger background
 187 temperature gradient decrease also show a larger decrease in variance. The skewness changes are

188 slightly more scattered (Fig. 6b), but the simplified equations generally capture the correct sign of
189 the skewness change and the model spread, with the models that predict a larger relative gradient
190 decrease to the north exhibiting a larger skewness increase than other models.

191 Following a similar argument, if the gradient changes to the north and south both reinforce
192 the original temperature gradient (i.e., $\frac{\Delta\bar{T}_{Ny}}{\bar{T}_{Ny}} > 0$ and $\frac{\Delta\bar{T}_{Sy}}{\bar{T}_{Sy}} > 0$) (as in the second case examined
193 for central Europe during summer), then from (3) the variance change is positive, while from (4)
194 the skewness change will again depend on the magnitude of the relative gradient changes. The
195 latter explains why a large model spread in skewness change is observed for central Europe during
196 summer, including a disagreement regarding the sign of the change (Fig. 5g), as some models
197 predict large relative gradient changes to the north, while others predict large changes to the south
198 (Fig. 6d). The simplified equations capture this well, including the correct sign of the projected
199 skewness change. There is only a weak correlation between the gradient and the variance increase
200 over central Europe during summer (Fig. 6c). The sign of the change is captured correctly by
201 the simplified equations, but it is clear that the meridional background temperature increase is not
202 the only factor controlling the variance increase. This is probably related to the fact that zonal
203 gradients are also important for this region during summer (Extended Data Fig. 4h), and also
204 because land-surface processes, such as interaction with soil-moisture, become more important
205 during summer^{1,5,34}. Note that for both winter and summer, the weaker correlation found in Fig. 6b
206 and 6c compared to Fig. 6d and 6a, respectively, may also reflect the smaller model spread in these
207 cases (i.e. there is less spread across models to be explained).

208 Finally, the expressions for the variance and skewness given in (1) and (2) can be used to
209 estimate the intensities of cold and warm temperature anomalies. It is easy to show that (see
210 section 4 in the Supplementary Information):

$$T_c \approx \sigma \left(1 - \frac{S}{2} \right) \quad (5)$$

211 and

$$T_w \approx \sigma \left(1 + \frac{S}{2} \right). \quad (6)$$

212 If the actual variance and skewness are used in (5) and (6), then the amplitude of the cold and
213 warm temperature anomalies can be estimated directly and compared with the tracking results. The
214 projected changes in these estimated intensities are shown in Figs. 6e-h, which recover well the
215 intensity changes found using the Lagrangian approach (Fig. 3). For example, these expressions
216 correctly capture the stronger reduction in the intensity of cold anomalies in most of the NH during
217 winter, and also correctly capture the increase of both types of anomalies over central Europe
218 during summer.

219 This study has examined the variability of lower tropospheric (850 hPa) temperature in order
220 to better isolate the role of large-scale horizontal advection. A basic mechanism for temperature
221 skewness generation by linear advection of nonuniform background temperature gradients is pre-
222 sented, and simple expressions are derived to relate variance and skewness changes to background
223 temperature gradient changes, which describe well the projected model changes.

224 However, it is well known that processes associated with snow or ice melting and land

225 cover also influence the surface temperature variability during winter^{18,35–38}. The relevance of
226 our 850 hPa level findings for surface temperature can be examined by inspecting the near-surface
227 (T2m) winter temperature response (Extended Data Fig. 7). Overall, the winter mean and variance
228 changes are similar between the two levels, but there are quite significant differences between the
229 850 hPa level and the surface temperature skewness changes (compare Extended Data Fig. 7c,f
230 with Fig. 2a,c). The projected winter skewness changes are similar in the midlatitudes, but a neg-
231 ative (rather than positive) skewness change is projected poleward of the 0°C temperature line
232 (Extended Data Fig. 7c,f). The negative skewness change was proposed to be a direct result of
233 snow and sea ice melting¹⁸. However, the origin of the positive midlatitude skewness change had
234 previously been unexplained. During summer, other processes such as soil-moisture interactions
235 are known to be extremely important for surface temperature variability and extremes^{34,35,39–42}.
236 It has also been shown that the correlation between atmospheric circulation and surface tempera-
237 ture variability is weaker in summer compared to winter⁴³. However, the overall structure of the
238 projected 850 hPa summer mean, variance, and skewness changes still resemble well the T2m
239 response (Extended Data Fig. 8) (except in the Arctic). This again points towards a purely dynam-
240 ical mechanism shaping the temperature variability changes, which does not involve the boundary
241 layer.

242 The current study therefore provides an important element in understanding midlatitude sur-
243 face temperature changes, by explaining and quantifying the fundamental role of advection and
244 warming patterns in shaping the variance and skewness changes. These are more cleanly revealed
245 by analyzing the 850 hPa level, where the dynamical contribution can be isolated. Examining the

246 relative importance of atmospheric circulation and regional land-surface feedbacks in shaping the
247 surface temperature variability response to climate change is left for further study.

248 **Methods**

249 **Data**

250 In this study we use the 6-hourly 850 hPa temperature field from 26 CMIP5 models (see
251 model list in Table S1 in the Supplementary Information). All models are forced by the represen-
252 tative concentration pathway 8.5 (RCP8.5) emissions scenario, and the r1i1p1 ensemble member
253 is used⁴⁴. The data covers a period of 19 years in the historical runs (1981–1999), which include
254 both the observed anthropogenic and natural atmospheric forcings, and 19 years in the projected
255 runs (2081–2099), in which the radiative forcing increases by about 8.5 W m^{-2} by year 2100. For
256 each model, the background climatology is defined for every 6-hourly time period as its average
257 over the 19 years, in order to remove both the diurnal and the seasonal cycle. Perturbations are
258 then defined as deviations from the 6-hourly climatology (for the historical and projected simula-
259 tions separately). The variance and skewness are calculated first for each model separately, and
260 then averaged together to produce the ensemble means. We concentrate on the NH during both the
261 winter (DJF) and summer (JJA) seasons.

262 To examine the accuracy of the historical CMIP5 data in reproducing the observed temper-
263 ature variability, we also analyze ERA-I reanalysis data⁴⁵ (Extended Data Fig. 2 and Extended
264 Data Fig. 3). We use the 6-hourly 850 hPa temperature field from the ECMWF ERA-I reanaly-

265 sis dataset, covering the years 1980-2014, where the background climatology is defined for every
266 6-hourly time period as its average over the 35 years.

267 **Tracking algorithm**

268 The current study employs the objective spherical feature-tracking algorithm TRACK^{46,47},
269 which is typically used for cyclone tracking, but is modified here to track temperature anomalies in-
270 stead. We track the 850 hPa temperature perturbations by subtracting the background state, defined
271 as the 6-hourly climatology (compared with the spatial filtering of the large scale background flow
272 that is usually applied for cyclones). The 6-hourly temperature anomaly field is then reduced to a
273 T42 grid to smooth the data and reduce noise. The positive and negative temperature anomalies are
274 identified as the maxima or minima of the anomaly field, respectively, that exceed a threshold of
275 0.5 K. The positive and negative centers are then tracked separately every 6 hours. This tracking is
276 performed directly on the sphere, and is achieved by first initializing the maxima or minima into a
277 set of tracks using a nearest neighbour method, and then refining these by performing a constrained
278 minimization of a cost function for track smoothness (formulated in spherical coordinates)⁴⁷. Only
279 features that last for more than two days are retained for the statistical calculations, which includes
280 semi-stationary features as well as the more mobile systems (so that more slowly propagating per-
281 turbations like heat waves can be identified too). The spatial statistics of the tracked anomalies
282 are then obtained using adaptive locally defined spherical kernel estimators, which are a form of
283 distance weighted statistical estimator⁴⁸. For example, the mean intensity at a certain grid point
284 is estimated from the intensity of adjacent track points using a decay function (the local spherical
285 kernel estimator), which depends on the distance between the track point and the gridpoint. The

286 kernel bandwidth, which controls the statistic smoothness, is adapted according to the data density.
287 This approach has the benefit of computing the statistics directly on the sphere which prevents the
288 introduction of biases that often occur for grid box methods. The spatial statistics are computed for
289 each model separately, and then averaged together.

290 **Regional composites**

291 The regional composites of the anomalous velocity associated with strong cold and warm
292 temperature anomalies are constructed using the tracking results of the 850 hPa temperature anoma-
293 lies. For each model, we first find the intensity of all the cold and warm anomalies that passed
294 through the region, keeping only the maximum value reached inside the region box. We then
295 find, for the cold and warm anomalies separately, the 75th percentile thresholds. The composites
296 of strong cold and warm anomalies are then constructed by averaging only over features whose
297 maximum intensity exceeds the 75th percentile (similar results are obtained when other percentile
298 thresholds are used instead). This is performed for each model separately, and the composites are
299 then averaged together, centered around the middle of the region box, for positive and negative
300 anomalies separately.

301 The meridional temperature gradients T_{N_y} and T_{S_y} used to estimate the variance and skew-
302 ness changes given by (3) and (4) (and shown in Figs. 6a-d) are calculated as the linear gradients
303 over four grid points to the north and to the south of the centers of each region box, respec-
304 tively. They are calculated for the seasonally averaged background temperature and hence are
305 time-independent.

306 **Statistical data analysis**

307 The Eulerian PDFs (presented in Figs. 4a and 5a) are calculated by accumulating all the
308 temperature anomalies (from all models) in a given region, and then adding the multi-model mean
309 temperature for the region. These are compared to the PDFs of intensity of anomalies from the
310 tracking (presented in Figs. 4b,c and 5b,c), calculated by accumulating all the positive and negative
311 features that pass through each region. The PDFs are obtained using a kernel fitting, and the
312 shading denotes the 95% confidence interval, calculated using a two-tailed t-distribution with 26
313 degrees of freedom ($t_s \approx 2.06$) and multiplying by the standard error of the mean model spread
314 (for each value of the PDF).

315 **Data availability**

316 The datasets analyzed in the current study were obtained from the World Data Center for
317 Climate (WDCC) repository, available at <http://cera-www.dkrz.de/WDCC/ui/>.

318 **Code availability**

319 The feature-tracking algorithm used in this study is available for download at <http://www.nerc-essc.ac.uk/kih/TRACK/Track.html>, by contacting Kevin Hodges (k.i.hodges@reading.ac.uk).

322 1. Schär, C. *et al.* The role of increasing temperature variability in European summer. *Nature*
323 **427**, 332–336 (2004).

324 2. Newman, W. I., Malamud, B. D. & Turcotte, D. L. Statistical properties of record-breaking

- 325 temperatures. *Phys. Rev. E* **82**, 066111 (2010).
- 326 3. Schneider, T., Bischoff, T. & Płotka, H. Physics of changes in synoptic midlatitude tempera-
327 ture variability. *J. Climate* **28**, 2312–2331 (2015).
- 328 4. Petoukhov, V., Eliseev, A. V., Klein, R. & Oesterle, H. On statistics of the free-troposphere
329 synoptic component: an evaluation of skewnesses and mixed third-order moments contribution
330 to the synoptic-scale dynamics and fluxes of heat and humidity. *Tellus A: Dynamic Meteorol-
331 ogy and Oceanography* **60**, 11–31 (2008).
- 332 5. Fischer, E. M. & Schär, C. Future changes in daily summer temperature variability: Driving
333 processes and role for temperature extremes. *Clim. Dyn.* **33**, 917–935 (2009).
- 334 6. Ruff, T. W. & Neelin, J. D. Long tails in regional surface temperature probability distributions
335 with implications for extremes under global warming. *Geophys. Res. Lett.* **39**, 1–6 (2012).
- 336 7. Perron, M. & Sura, P. Climatology of non-Gaussian atmospheric statistics. *J. Climate* **26**,
337 1063–1083 (2013).
- 338 8. Kodra, E. & Ganguly, A. R. Asymmetry of projected increases in extreme temperature distri-
339 butions. *Sci. Rep.* **4**, 5884 (2014).
- 340 9. Sardeshmukh, P. D., Compo, G. P. & Penland, C. Need for caution in interpreting extreme
341 weather statistics. *J. Climate* **28**, 9166–9187 (2015).

- 342 10. Garfinkel, C. I. & Harnik, N. The non-Gaussianity and spatial asymmetry of temperature
343 extremes relative to the storm track: The role of horizontal advection. *J. Climate* **30**, 445–464
344 (2017).
- 345 11. Loikith, P. C. & Neelin, J. D. Non-Gaussian cold-side temperature distribution tails and asso-
346 ciated synoptic meteorology. *J. Climate* **32**, 8399–8414 (2019).
- 347 12. Linz, M., Chen, G., Zhang, B. & Zhang, P. A framework for understanding how dynamics
348 shape temperature distributions. *Geophys. Res. Lett.* **47**, e2019GL085684 (2020).
- 349 13. Loikith, P. C. & Broccoli, A. J. Characteristics of observed atmospheric circulation patterns
350 associated with temperature extremes over North America. *J. Climate* **25**, 7266–7281 (2012).
- 351 14. Donat, M. G. & Alexander, L. V. The shifting probability distribution of global daytime and
352 night-time temperatures. *Geophys. Res. Lett.* **39**, L14707 (2012).
- 353 15. Volodin, E. M. & Yurova, A. Y. Summer temperature standard deviation, skewness and strong
354 positive temperature anomalies in the present day climate and under global warming condi-
355 tions. *Clim. Dyn.* **40**, 1387–1398 (2013).
- 356 16. Huybers, P., McKinnon, K. A., Rhines, A. & Tingley, M. U.S. daily temperatures: The mean-
357 ing of extremes in the context of nonnormality. *J. Climate* **27**, 7368–7384 (2014).
- 358 17. Diao, Y., Xie, S.-P. & Luo, D. Asymmetry of winter European surface air temperature ex-
359 tremes and the North Atlantic Oscillation. *J. Climate* **28**, 517–530 (2015).

- 360 18. Gao, Y., Leung, L. R., Lu, J. & Masato, G. Persistent cold air outbreaks over North America
361 in a warming climate. *Environ. Res. Lett.* **10**, 044001 (2015).
- 362 19. Loikith, P. C. *et al.* Surface temperature probability distributions in the NARCCAP hindcast
363 experiment: evaluation methodology, metrics, and results. *J. Climate* **28**, 978–997 (2015).
- 364 20. Bindoff, N. L. *et al.* Detection and attribution of climate change: from global to regional.
365 *Climate Change 2013: The Physical Science Basis. Contribution of Working Group I to the*
366 *Fifth Assessment Report of the Intergovernmental Panel on Climate Change* (2013).
- 367 21. Field, C. *et al.* (eds.) *IPCC, 2012: Managing the Risks of Extreme Events and Disasters to*
368 *Advance Climate Change Adaptation. A Special Report of Working Groups I and II of the*
369 *Intergovernmental Panel on Climate Change* (Cambridge University Press, Cambridge, UK,
370 and New York, NY, USA, 2012).
- 371 22. Screen, J. A. Arctic amplification decreases temperature variance in northern mid- to high-
372 latitudes. *Nat. Clim. Change.* **4**, 577–582 (2014).
- 373 23. Parey, S., Hoang, T. T. H. & Dacunha-Castelle, D. The importance of mean and variance in
374 predicting changes in temperature extremes. *J. Geophys. Res. Atmos.* **118**, 8285–8296 (2013).
- 375 24. Holmes, C. R., Woollings, T., Hawkins, E. & de Vries, H. Robust future changes in temper-
376 ature variability under greenhouse gas forcing and the relationship with thermal advection. *J.*
377 *Climate* **29**, 2221–2236 (2016).
- 378 25. Ballester, J., Giorgi, F. & Rodó, X. Changes in European temperature extremes can be pre-
379 dicted from changes in PDF central statistics. *Climatic Change* **98**, 277–284 (2009).

- 380 26. McKinnon, K. A., Rhines, A., Tingley, M. P. & Huybers, P. The changing shape of North-
381 ern Hemisphere summer temperature distributions. *J. Geophys. Res. Atmos.* **121**, 8849–8868
382 (2016).
- 383 27. Lewis, S. C. & King, A. D. Evolution of mean, variance and extremes in 21st century temper-
384 atures. *Weather and Climate Extremes* **15**, 1–10 (2017).
- 385 28. Tamarin-Brodsky, T., Hodges, K., Hoskins, B. J. & Shepherd, T. G. A dynamical perspective
386 on atmospheric temperature variability and its response to climate change. *J. Climate* **32**,
387 1707–1724 (2019).
- 388 29. Linz, M., Chen, G. & Hu, Z. Large-scale atmospheric control on non-Gaussian tails of mid-
389 latitude temperature distributions. *Geophys. Res. Lett.* **45**, 9141–9149 (2018).
- 390 30. Stocker, T. *et al.* *Climate Change 2013 - The Physical Science Basis. Contribution of Working*
391 *Group I to the Fifth Assessment Report of the Intergovernmental Panel on Climate Change*
392 (Cambridge University Press, Cambridge, UK, and New York, USA, 2014).
- 393 31. Fischer, E. M., Rajczak, J. & Schär, C. Changes in European summer temperature variability
394 revisited. *Geophys. Res. Lett.* **39**, L19702 (2012).
- 395 32. Hoskins, B. & Hodges, K. New perspectives on the Northern Hemisphere winter storm tracks.
396 *J. Atmos. Sci.* **59**, 1041–1061 (2002).
- 397 33. Lutsko, N. J., Baldwin, J. W. & Cronin, T. W. The impact of large-scale orography on northern
398 hemisphere winter synoptic temperature variability. *J. Climate* **32**, 5799–5814 (2019).

- 399 34. Seneviratne, S. I., Lüthi, D., Litschi, M. & Schär, C. Land-atmosphere coupling and climate
400 change in Europe. *Nature* **443**, 205–209 (2006).
- 401 35. Gregory, J. M. & Mitchell, J. F. Simulation of daily variability of surface temperature and
402 precipitation over Europe in the current and 2xCO₂ climates using the UKMO climate model.
403 *Q. J. R. Meteorol. Soc.* **121**, 1451–1476 (1995).
- 404 36. Cohen, J. & Entekhabi, D. The influence of snow cover on northern hemisphere climate
405 variability. *Atmosphere - Ocean* **39**, 35–53 (2001).
- 406 37. Findell, K. L. *et al.* The impact of anthropogenic land use and land cover change on regional
407 climate extremes. *Nat. Commun.* **8**, 989 (2017).
- 408 38. Diro, G. T., Sushama, L. & Huziy, O. Snow-atmosphere coupling and its impact on tempera-
409 ture variability and extremes over North America. *Climate Dynamics* **50**, 2993–3007 (2018).
- 410 39. Lenderink, G., Van Ulden, A., Van Den Hurk, B. & Van Meijgaard, E. Summertime inter-
411 annual temperature variability in an ensemble of regional model simulations: Analysis of the
412 surface energy budget. *Climatic Change* **81**, 233–247 (2007).
- 413 40. Fischer, E. M., Lawrence, D. M. & Sanderson, B. M. Quantifying uncertainties in projections
414 of extremes-a perturbed land surface parameter experiment. *Climate Dynamics* **37**, 1381–1398
415 (2011).
- 416 41. Berg, A. *et al.* Impact of soil moisture atmosphere interactions on surface temperature distri-
417 bution. *J. Climate* **27**, 7976–7993 (2014).

- 418 42. Douville, H., Colin, J., Krug, E., Cattiaux, J. & Thao, S. Midlatitude daily summer tem-
419 peratures reshaped by soil moisture under climate change. *Geophys. Res. Lett.* **43**, 812–818
420 (2016).
- 421 43. Vautard, R. & Yiou, P. Control of recent European surface climate change by atmospheric
422 flow. *Geophys. Res. Lett.* **36**, 6–11 (2009).
- 423 44. Taylor, K., Stouffer, R. & Meehl, G. An overview of CMIP5 and the experiment design. *Bull.*
424 *Amer. Meteor. Soc.* **93**, 485–498 (2012).
- 425 45. Dee, D. P. *et al.* The ERA-Interim reanalysis: configuration and performance of the data
426 assimilation system. *Q. J. R. Meteorol. Soc.* **137**, 553–597 (2011).
- 427 46. Hodges, K. I. Feature tracking on the unit sphere. *Mon. Weather Rev.* **123**, 3458–3465 (1995).
- 428 47. Hodges, K. I. Adaptive constraints for feature tracking. *Mon. Weather Rev.* **127**, 1362–1373
429 (1999).
- 430 48. Hodges, K. I. Spherical nonparametric estimators applied to the UGAMP model integration
431 for AMIP. *Mon. Weather Rev.* **124**, 2914–2932 (1996).

432 **Acknowledgements** This research has been supported by the James S. McDonnell Foundation for com-
433 plex systems, and by the European Research Council Advanced Grant (ACRCC) “Understanding the atmo-
434 spheric circulation response to climate change”, project 339390. The data were obtained from the World
435 Data Center for Climate (WDCC). We acknowledge the World Climate Research Programme’s Working
436 Group on Coupled Modelling, which is responsible for CMIP, and we thank the climate modeling groups

437 (listed in Table S1 of the SI) for producing and making available their model output. For CMIP the U.S.
438 Department of Energy's Program for Climate Model Diagnosis and Intercomparison provides coordinating
439 support and led development of software infrastructure in partnership with the Global Organization for Earth
440 System Science Portals.

441 **supplementary information** Extended Data and Supplementary Information accompany this paper.

442 **Author Contributions** T.T.B., K.H., B.J.H. and T.G.S. designed the study and wrote the paper; T.T.B
443 performed the data analyses.

444 **Competing Interests** The authors declare that they have no competing financial interests.

445 **Correspondence** Correspondence and requests for materials should be addressed to T. Tamarin-Brodsky
446 (email: t.tamarin@reading.ac.uk).

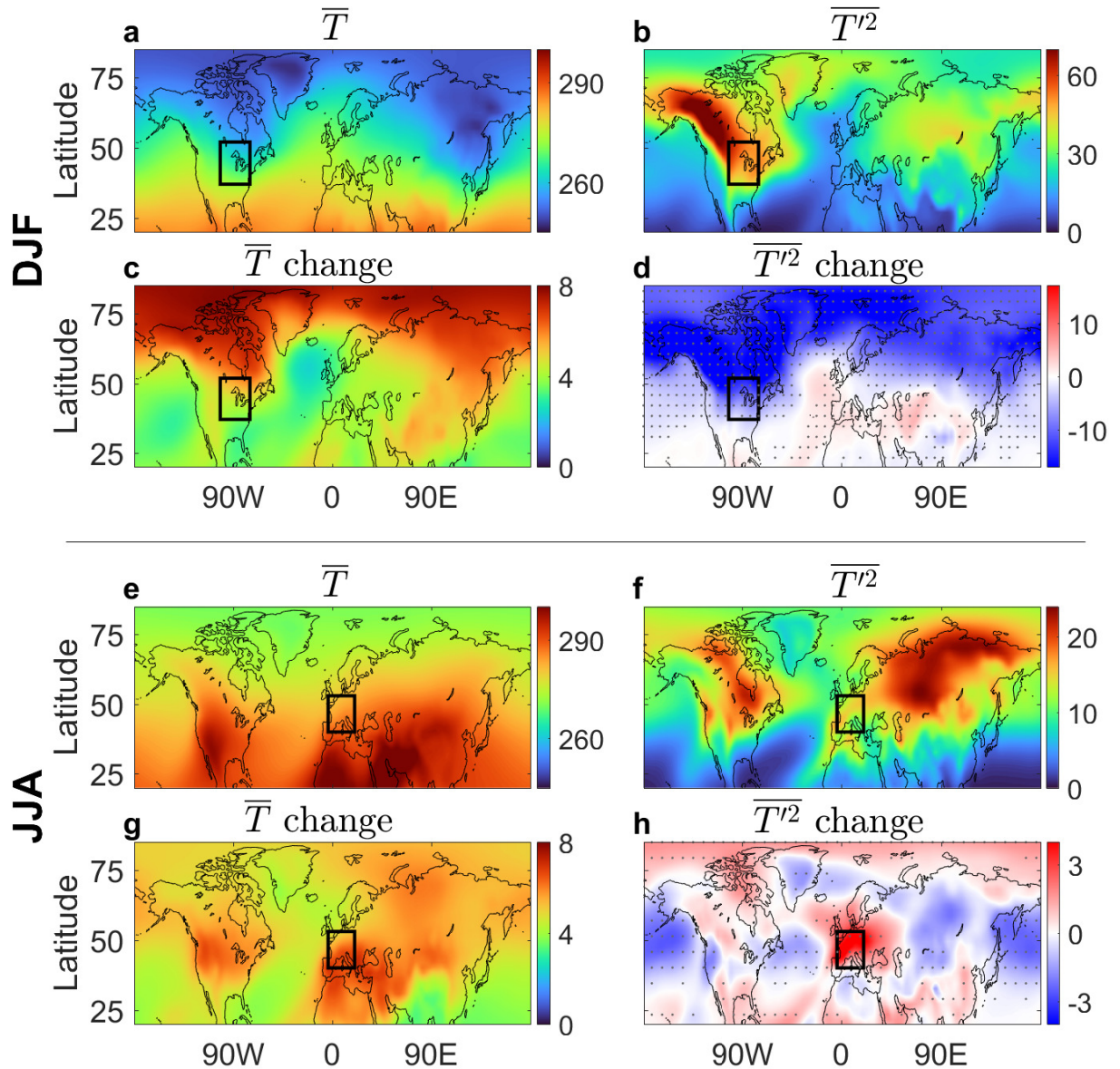


Figure 1: The historical (1981-1999) ensemble-mean climatological temperature and variance and their projected changes (2081-2099 minus historical), based on 26 CMIP5 RCP8.5 ensemble members. The 850 hPa (a) mean temperature (K) and (b) temperature variance (K²) during winter (December-January, DJF), and the corresponding projected changes in (c) and (d), respectively. Panels (e)-(h) show the same but for the summer period (June-August, JJA). Regions where more than 70% of the models agree on the sign of the variance changes are stippled.

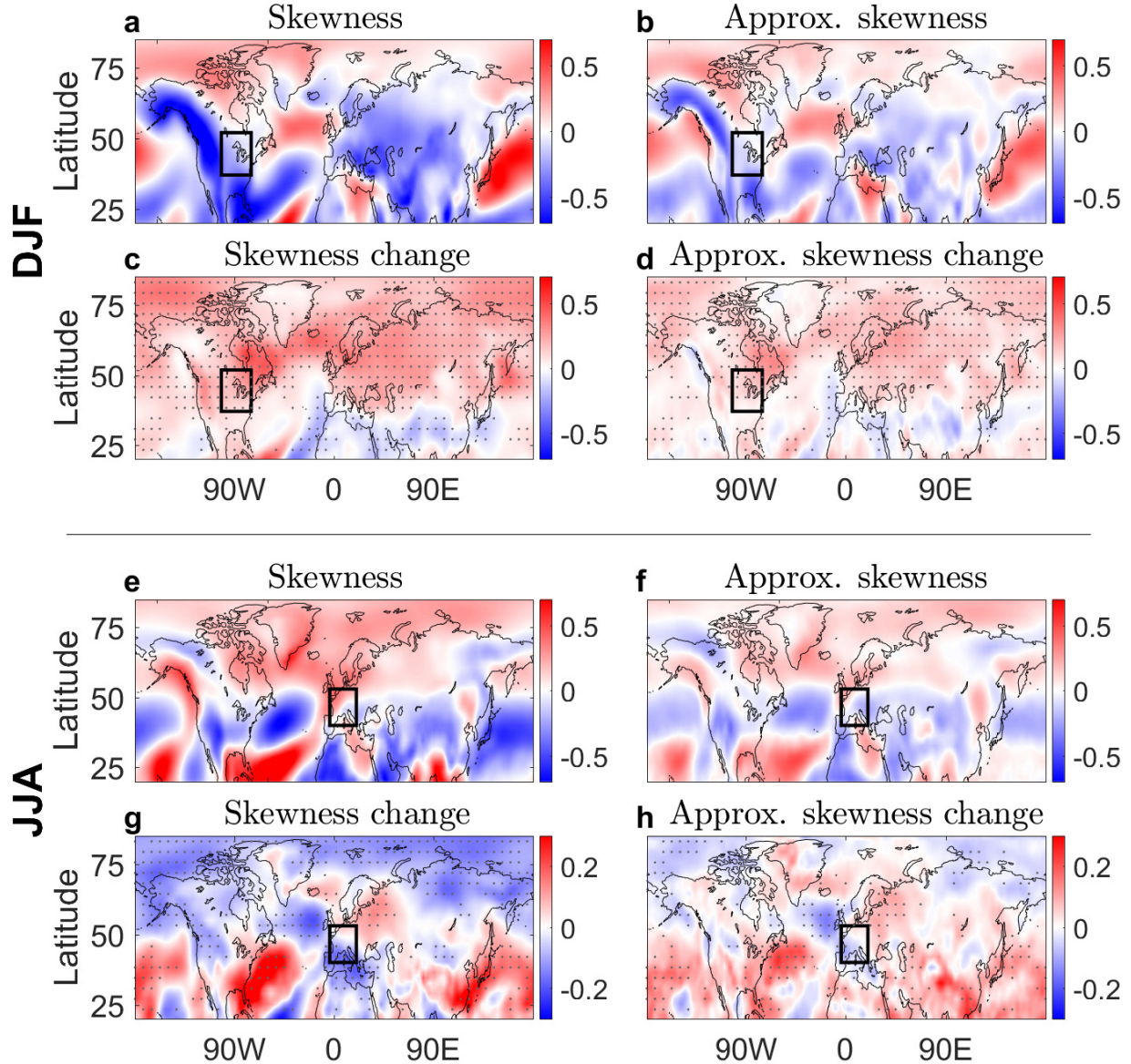


Figure 2: The historical (1981-1999) ensemble-mean temperature skewness and its projected changes (2081-2099 minus historical). The 850 hPa winter (DJF) (a) temperature skewness and (b) approximate temperature skewness, $S \approx \frac{T_w - T_c}{\frac{1}{2}(T_w + T_c)}$ (see Supplementary Information), where T_c and T_w denote the mean intensity (in absolute value) of the cold and warm temperature anomalies, respectively, produced from the tracking statistics (see Methods and Fig. 3). The corresponding projected changes are shown in (c) and (d), respectively. Panels (e)-(h) show the same but for the summer period (JJA). Regions where more than 70% of the models agree on the sign of the changes are stippled.

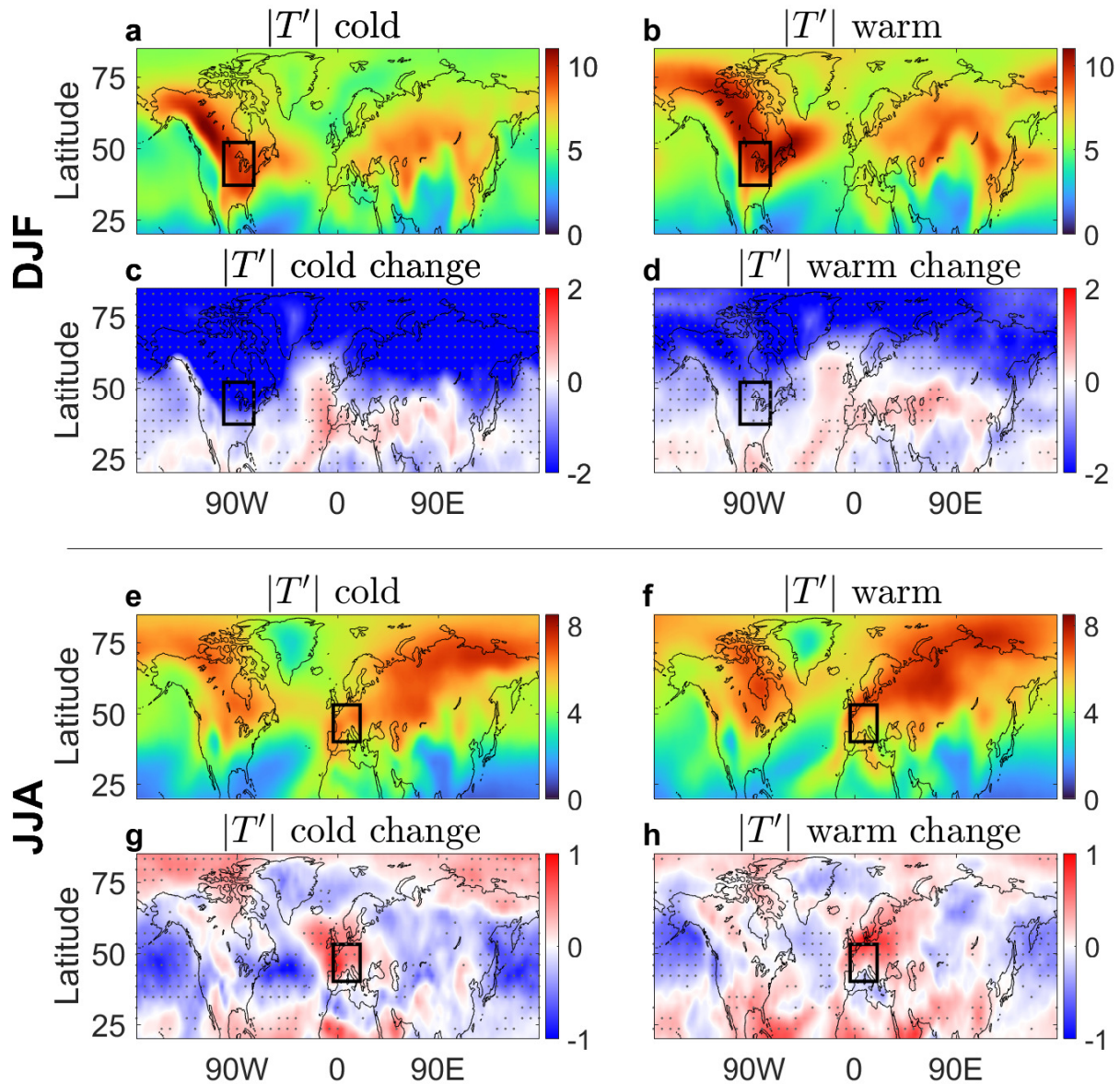


Figure 3: The historical (1981-1999) ensemble-mean intensities of cold and warm anomalies produced from the temperature tracking statistics, and their projected changes (2081-2099 minus historical). The mean intensity of the 850 hPa (a) cold and (b) warm temperature anomalies during winter (DJF), and their corresponding projected changes in (c) and (d), respectively. Panels (e)-(h) show the same but for the summer period (JJA). Regions where more than 70% of the models agree on the sign of the changes are stippled.

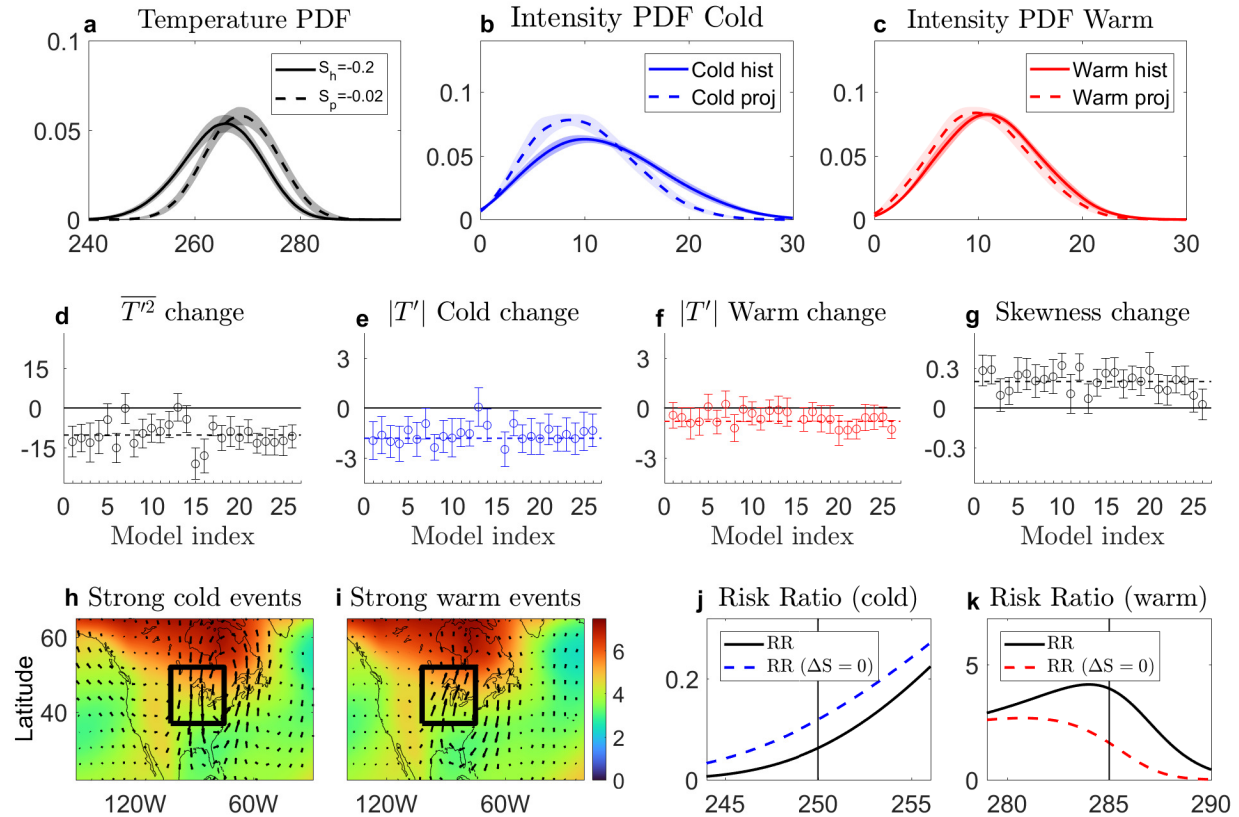


Figure 4: The 850 hPa temperature variability changes in east-central North America during DJF. PDF of (a) temperature (K), and intensity of (b) cold and (c) warm temperature anomalies (K) from the tracking, for the historical (solid lines) and projected (dashed lines) simulations (S_h and S_p in the legend of (a) denote the corresponding skewness of the PDF). The model spread of the region-averaged (d) temperature variance (K^2), (e) intensity of cold and (f) warm temperature anomalies (K) from the tracking statistics, and (g) temperature skewness, where each dot corresponds to a model in accordance with the list in Table S1. Dashed horizontal lines show the ensemble mean averages, and the errorbars denote the 95% confidence interval from the yearly values for each model. Composites of the anomalous circulation (arrows) in the projected simulations associated with strong (h) cold and (i) warm anomalies that crossed the region (see Methods), and the projected background temperature increase (shading). Black box denotes the region. The risk ratio of the (j) cold and (k) warm tails, with (solid black line) or without (dashed lines) the projected skewness change.

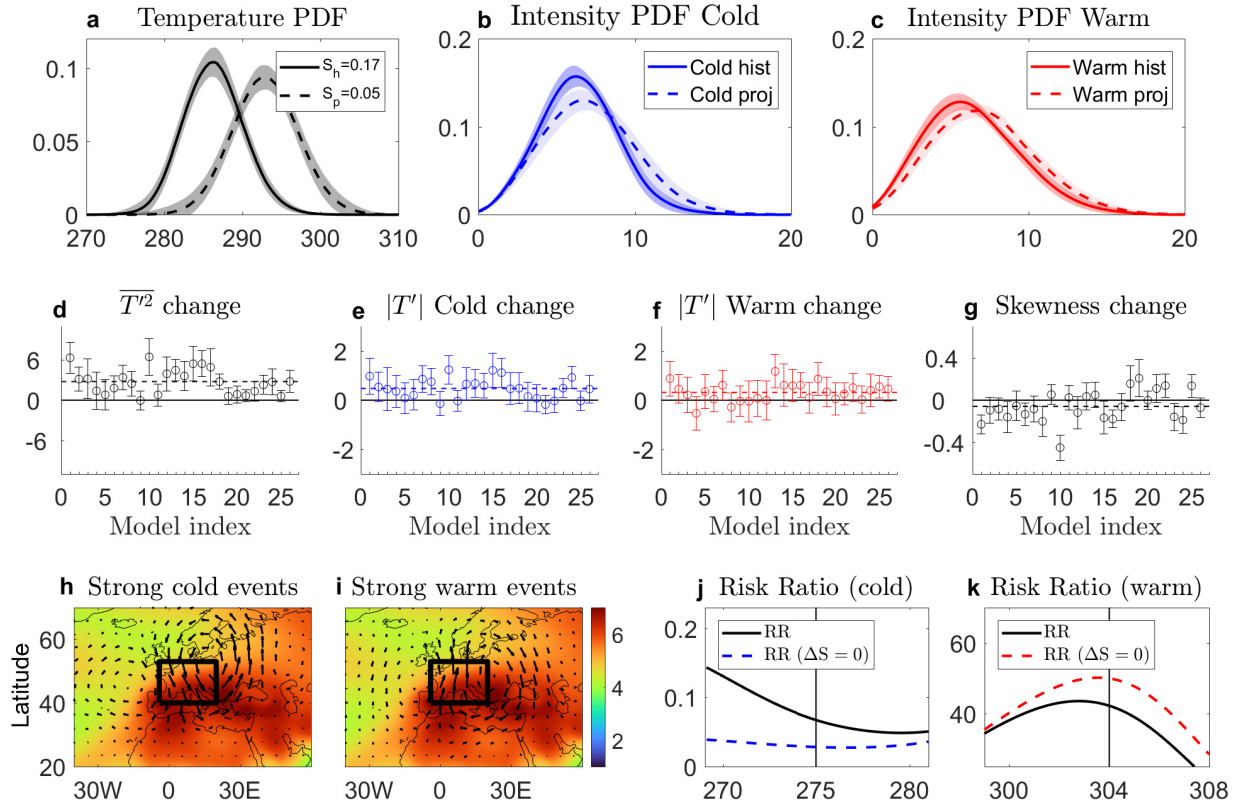


Figure 5: As in Fig. 4 but for central Europe during summer (JJA).

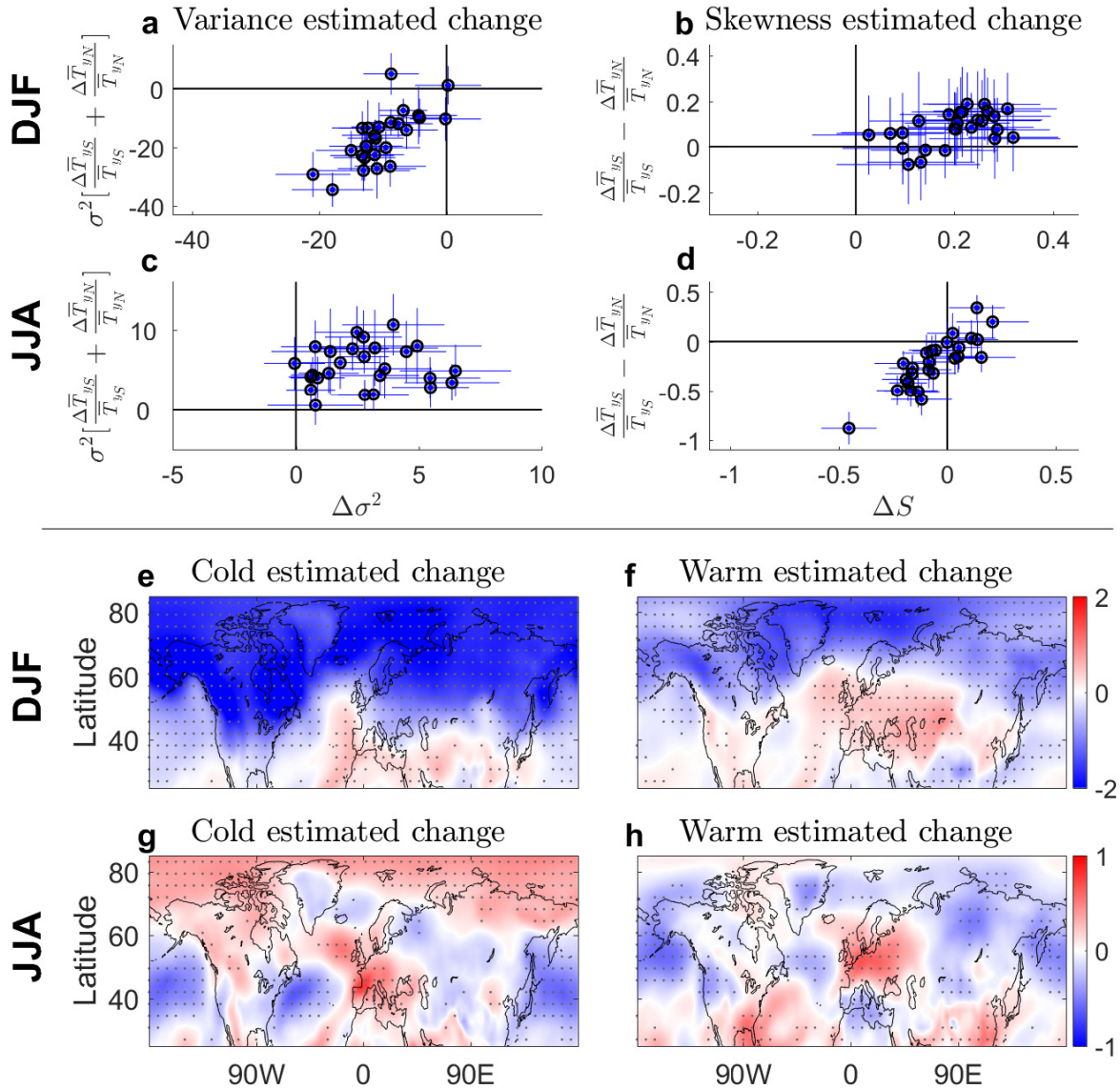
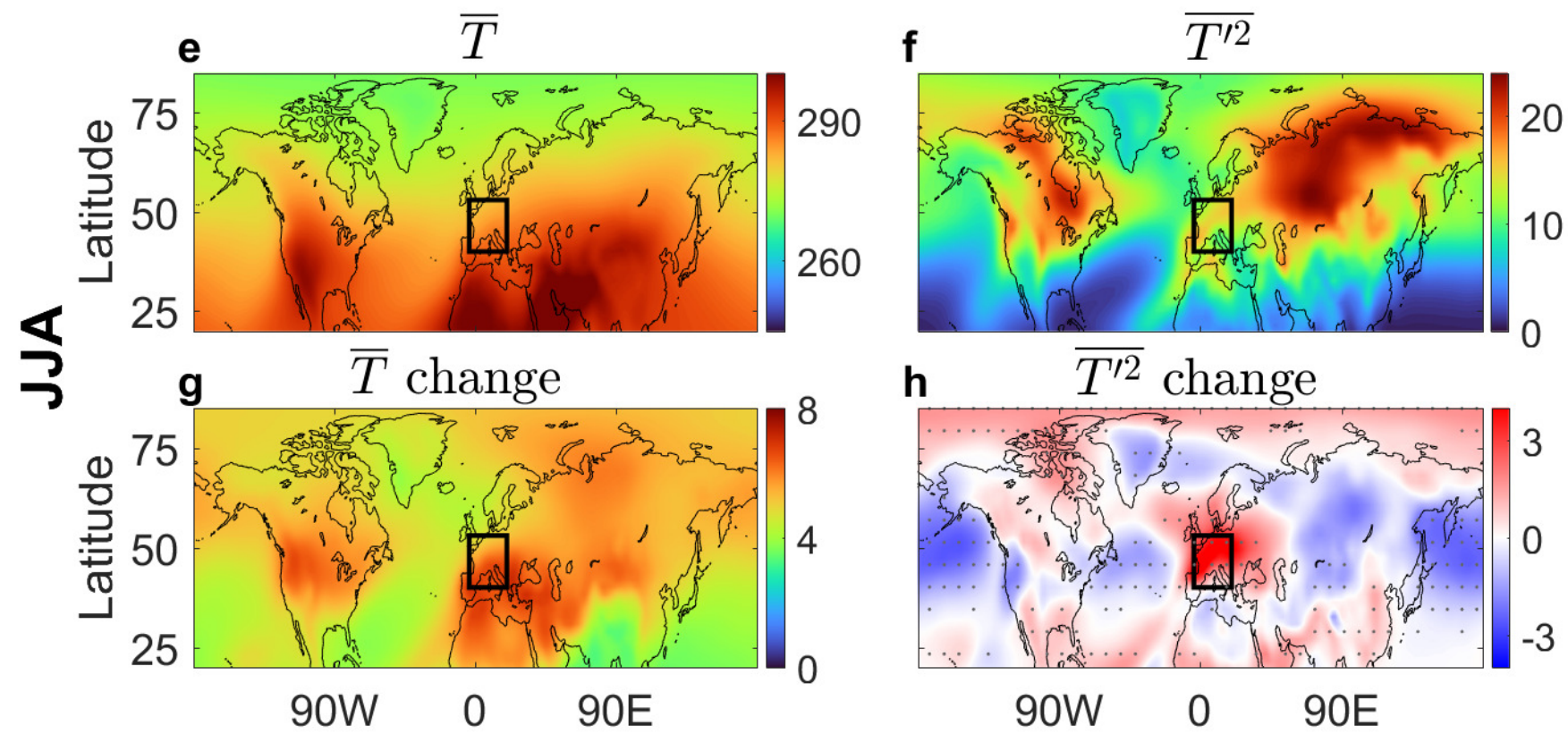
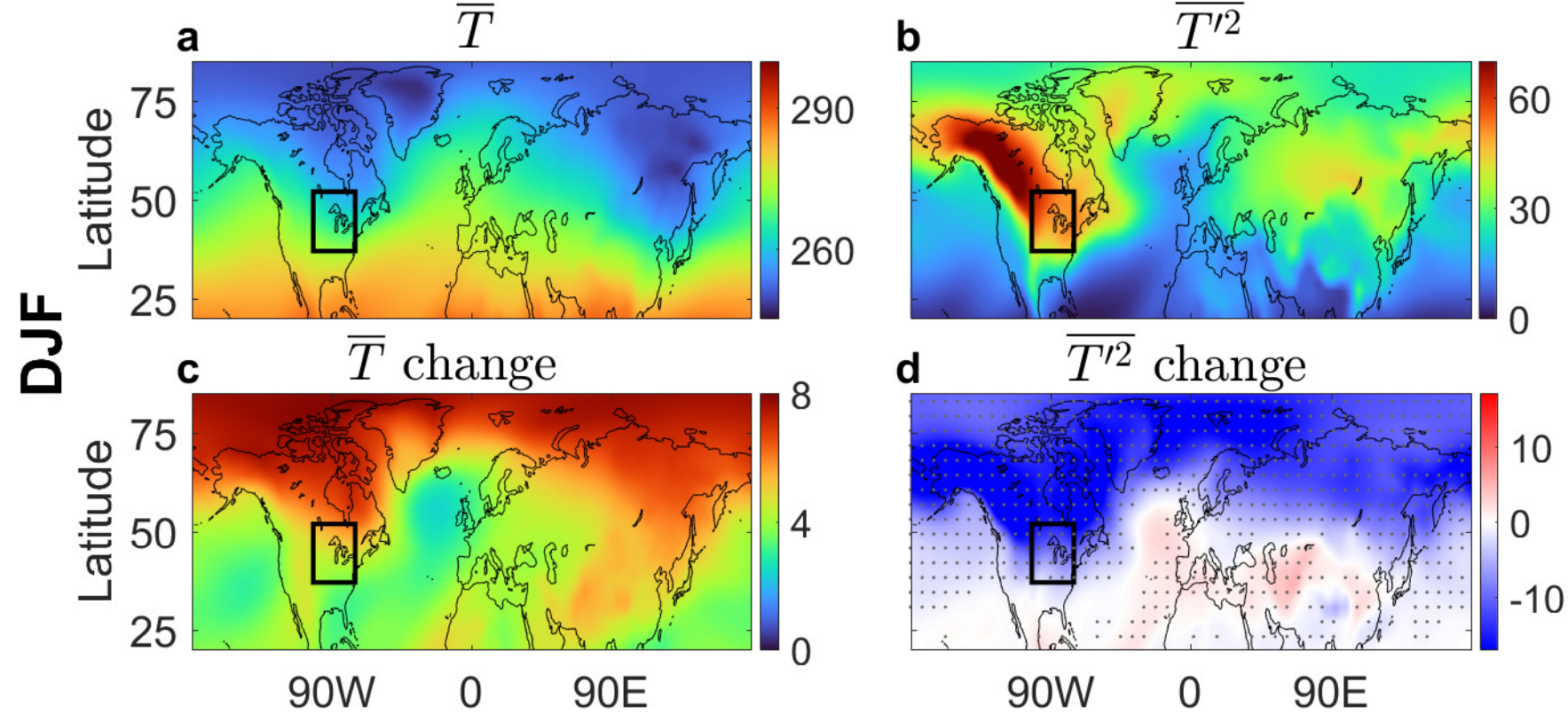
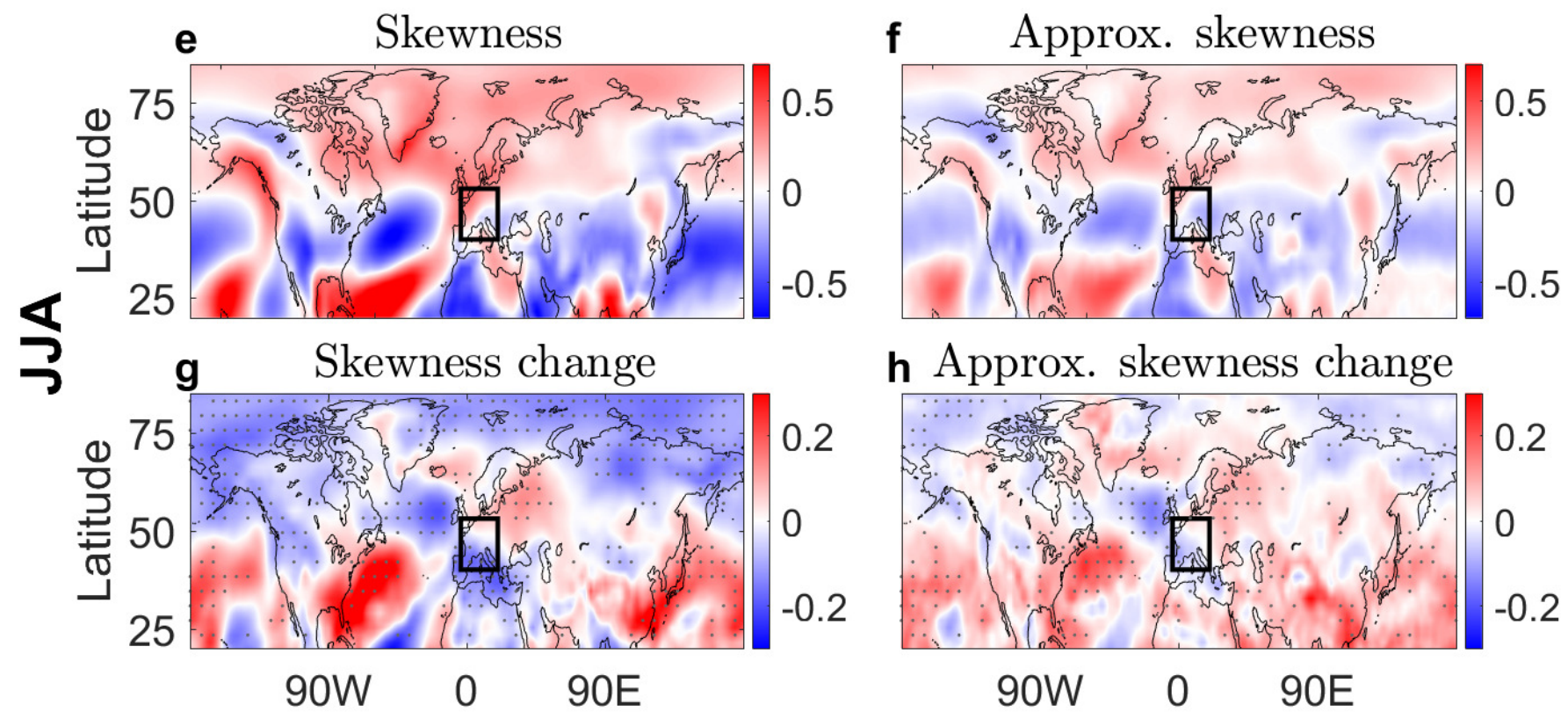
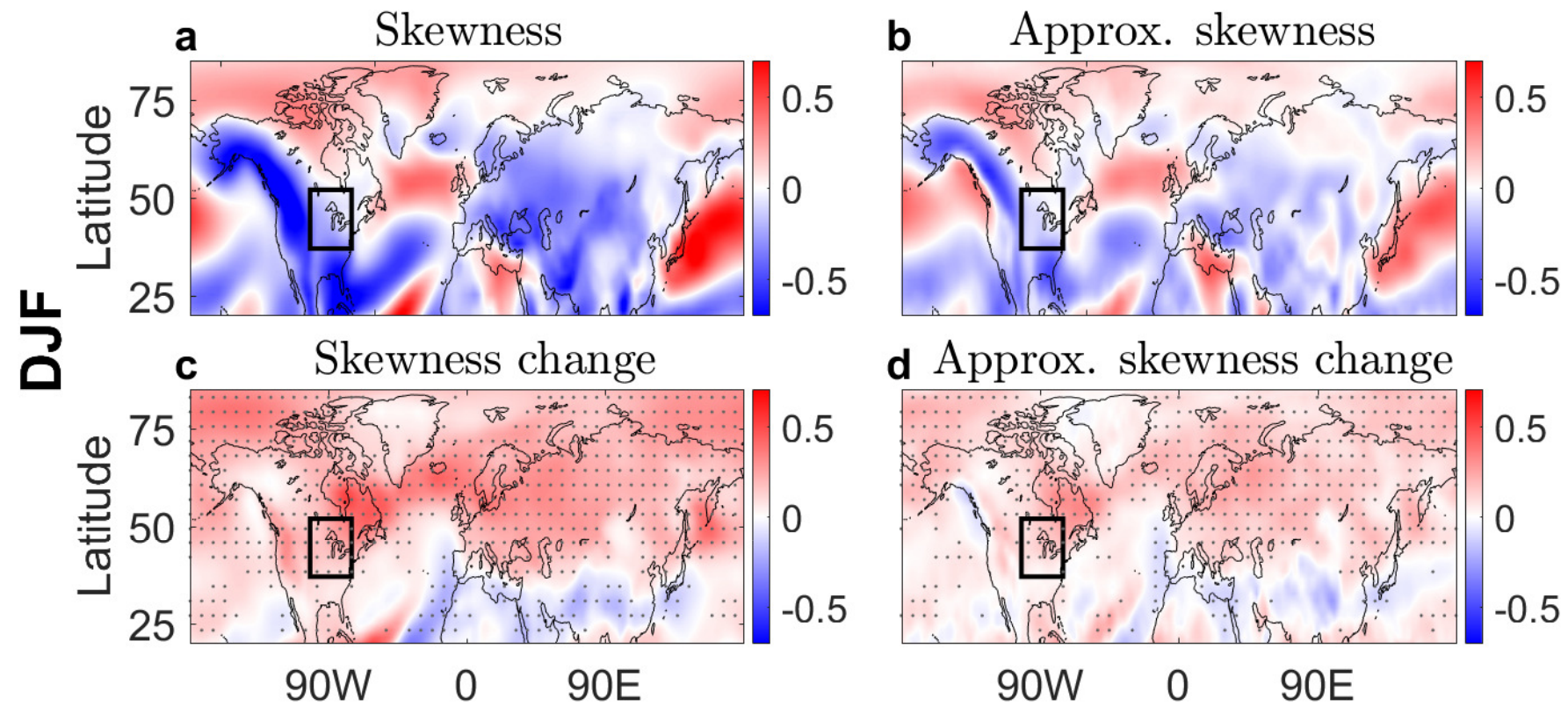
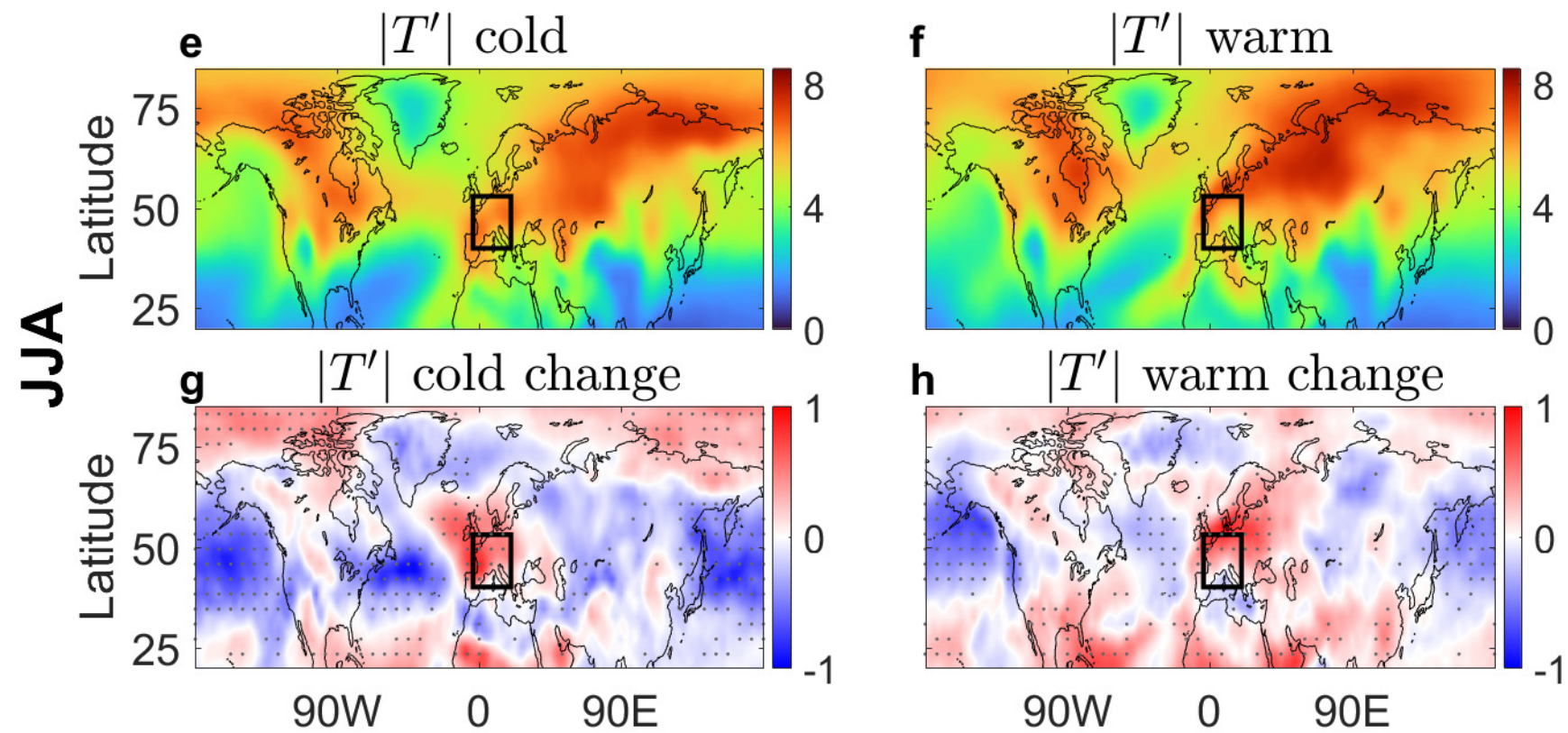
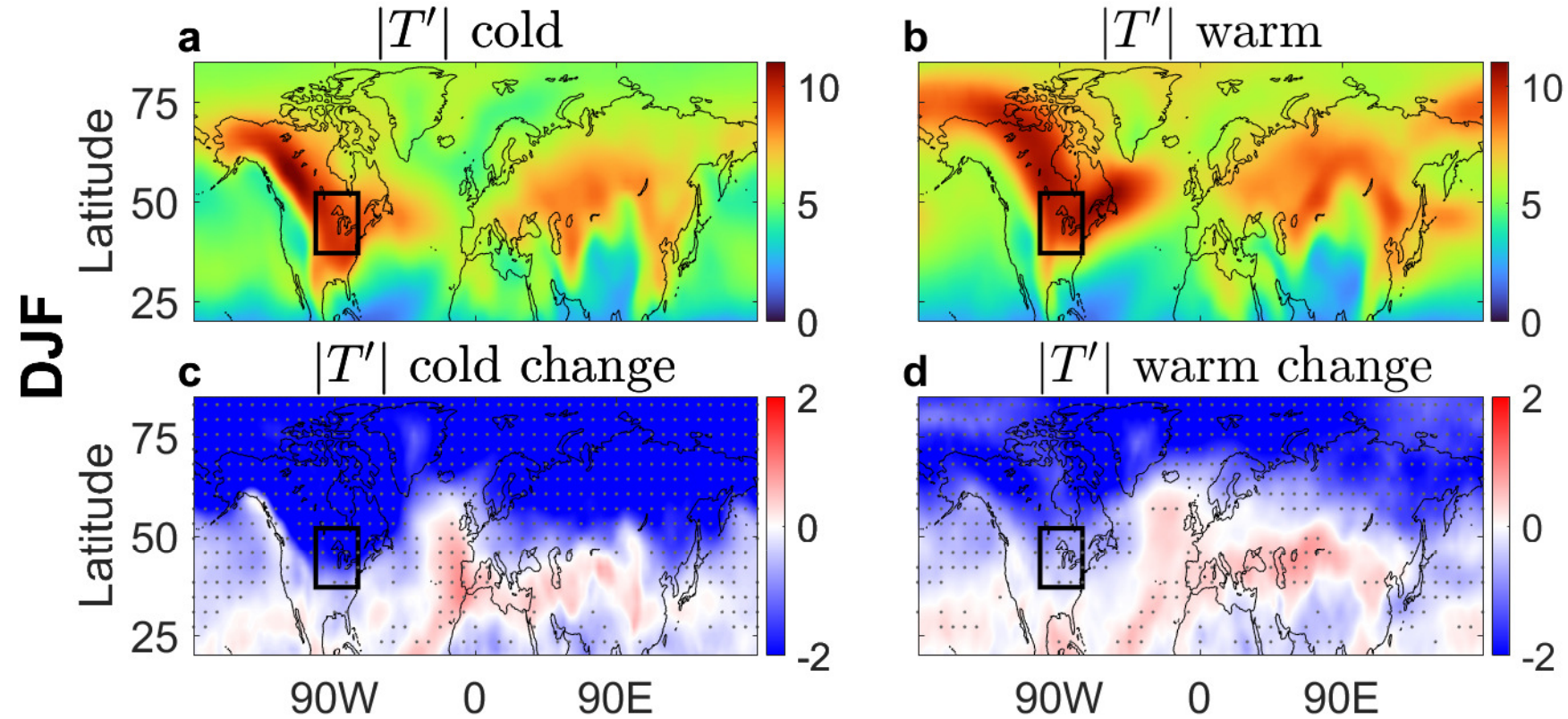
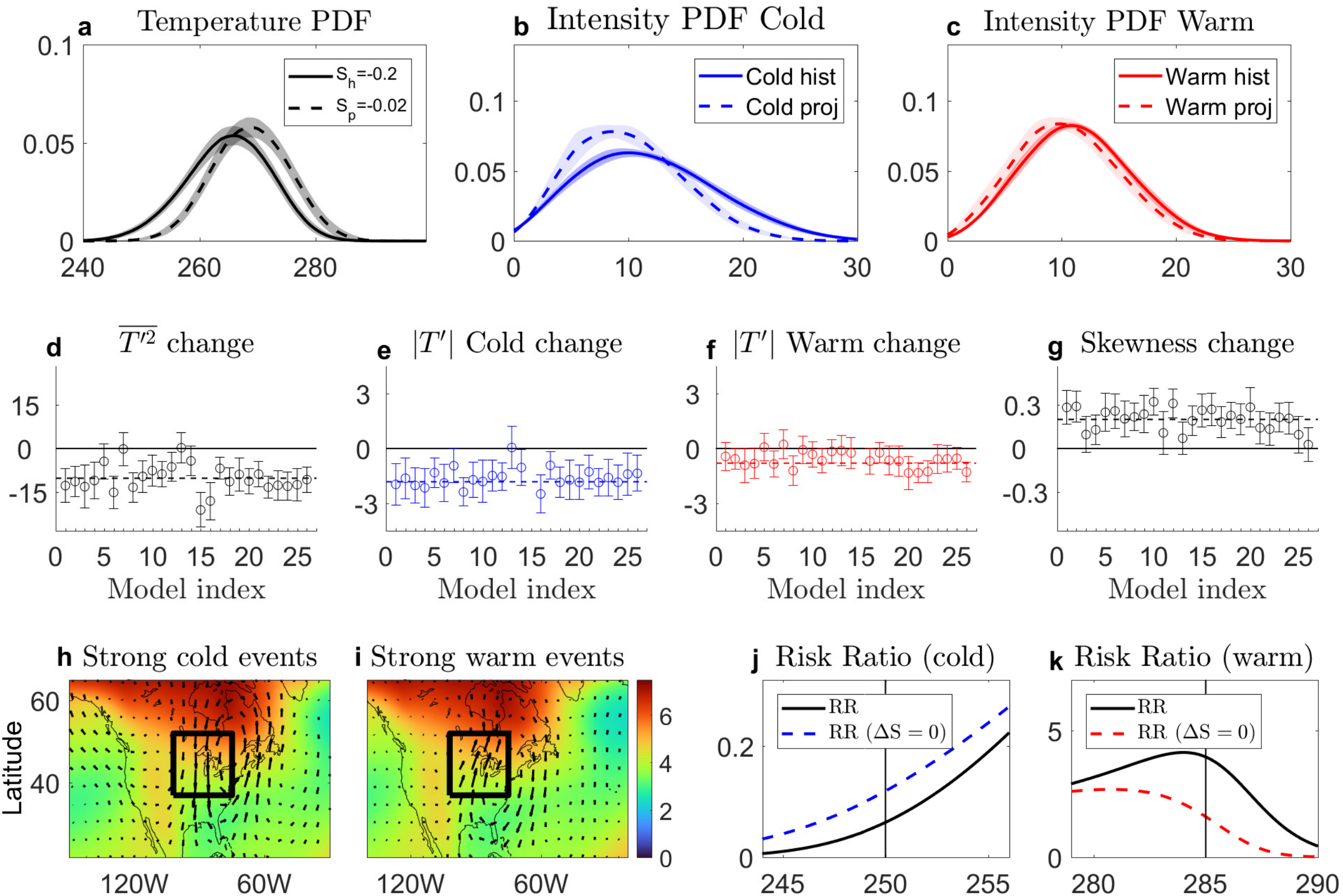


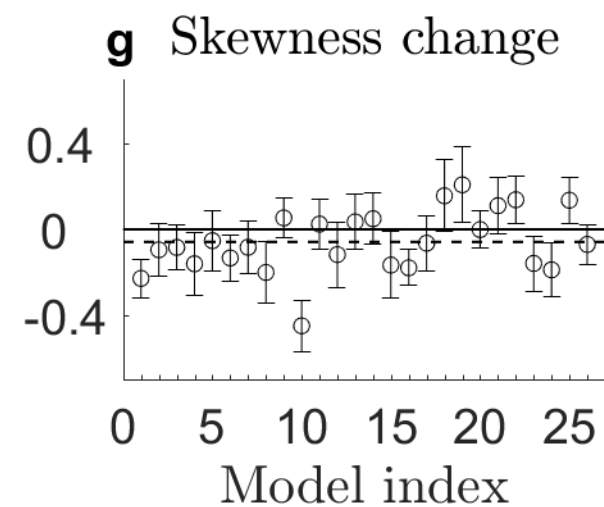
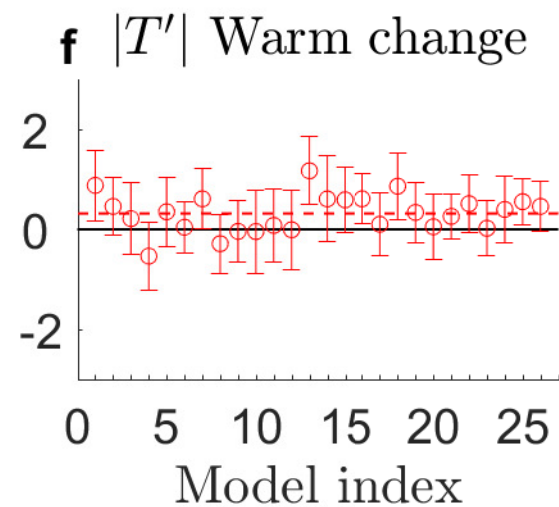
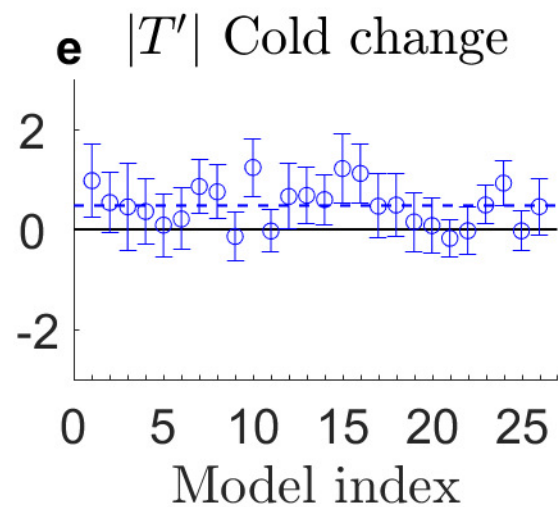
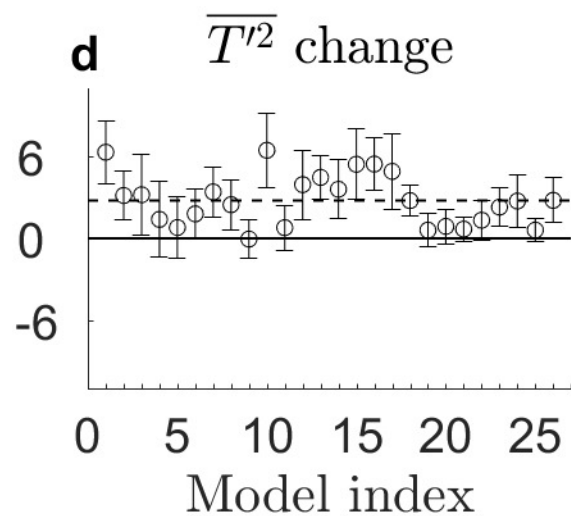
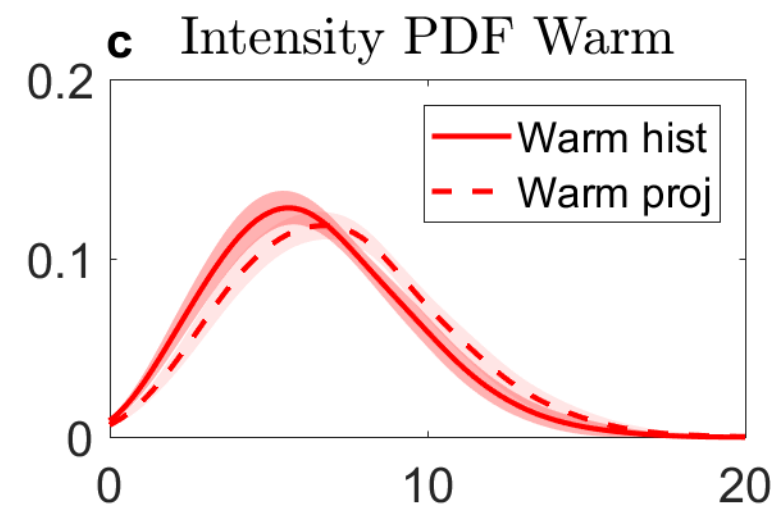
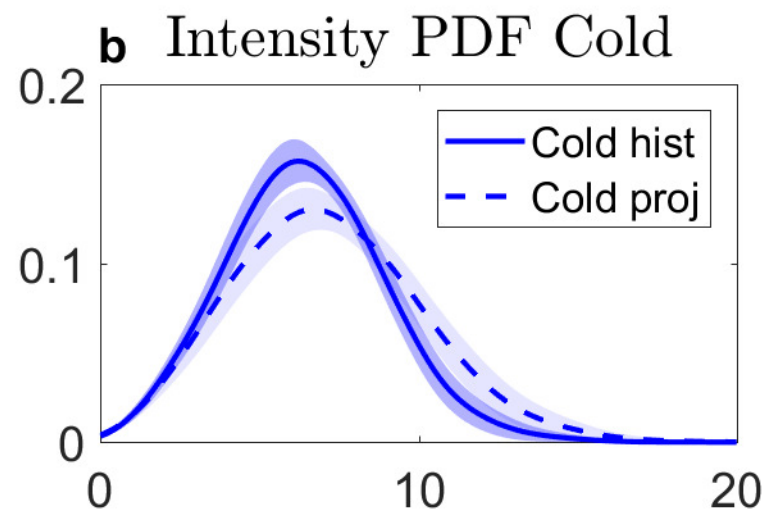
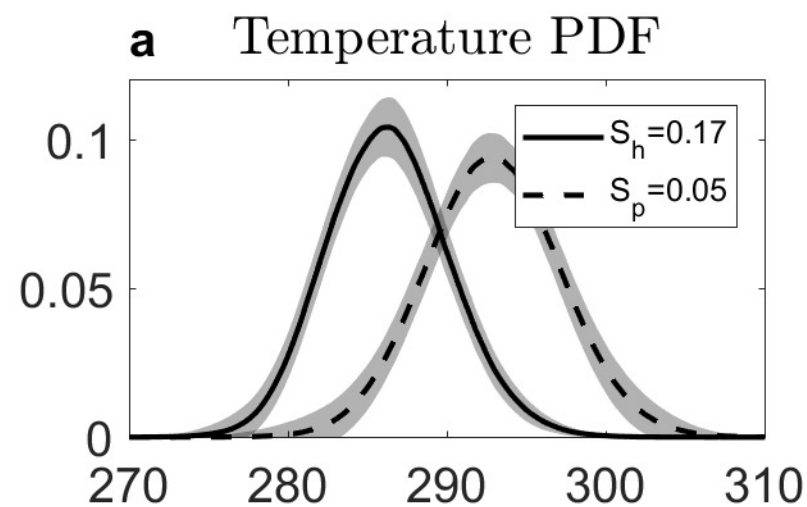
Figure 6: Estimated temperature variance and skewness changes, and estimated changes in the mean intensity of cold and warm anomalies. The predicted vs. simulated variance (a,c) and skewness (b,d) changes for east-central North America during winter (first row) and central Europe during summer (second row). Each dot represents a model, and the errorbars denote the 95% confidence intervals from the yearly values. Ensemble-mean estimated changes in the intensity of (e) cold and (f) warm anomalies during winter (DJF), and of (g) cold and (h) warm anomalies during summer (JJA). The approximations are based on the spatial distribution of variance and skewness, and given by projected changes of (5) and (6) for the cold and warm anomalies, respectively. Regions where more than 70% of the models agree on the sign of the changes are stippled.





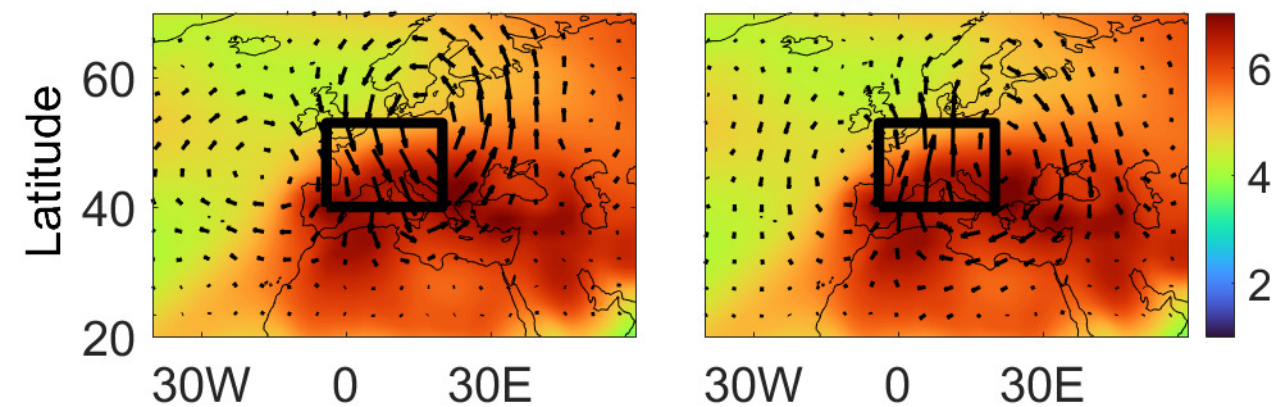




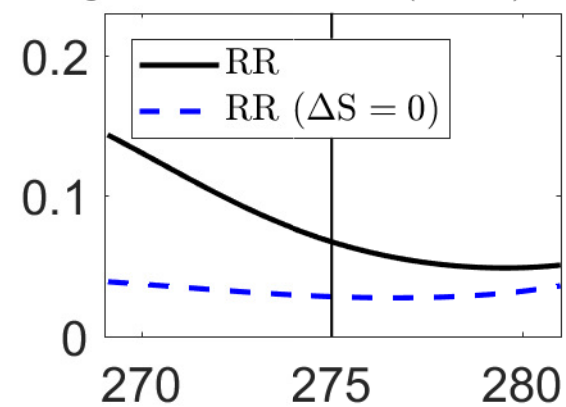


h Strong cold events

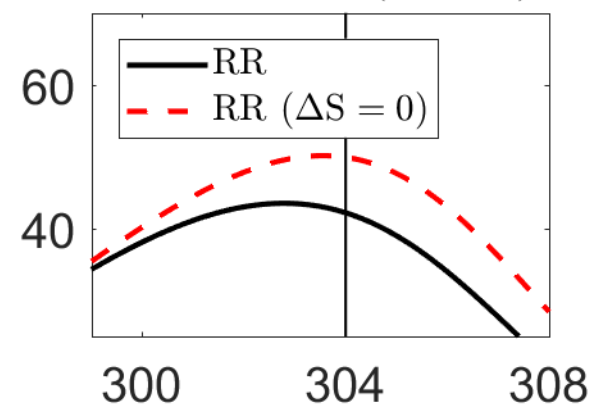
i Strong warm events



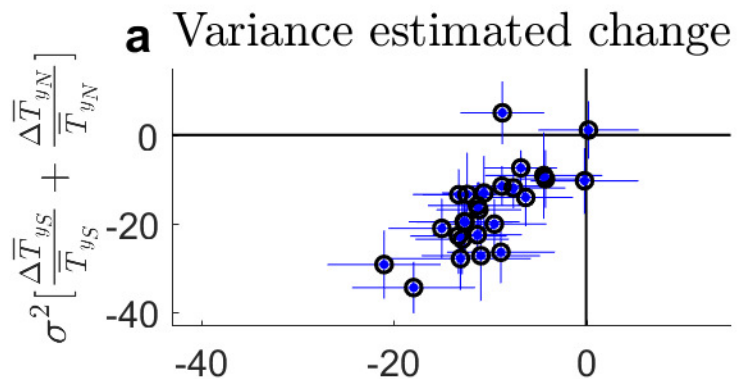
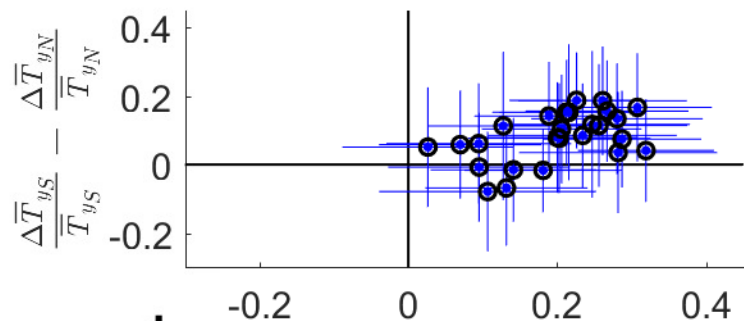
j Risk Ratio (cold)



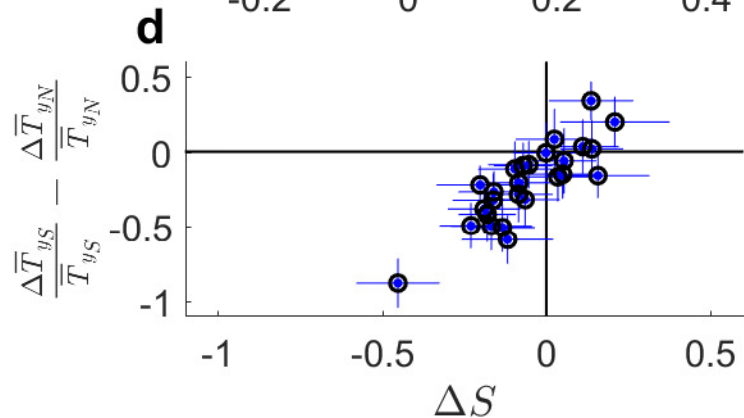
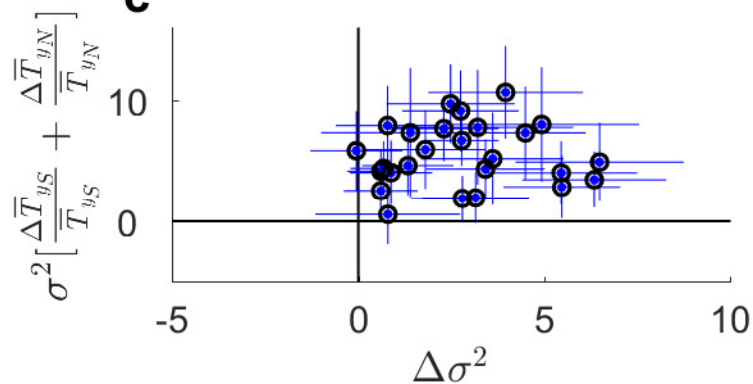
k Risk Ratio (warm)



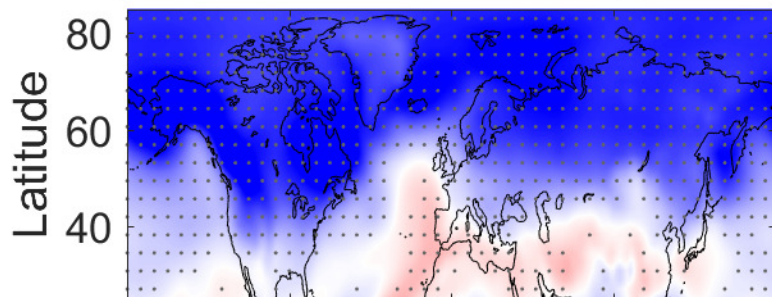
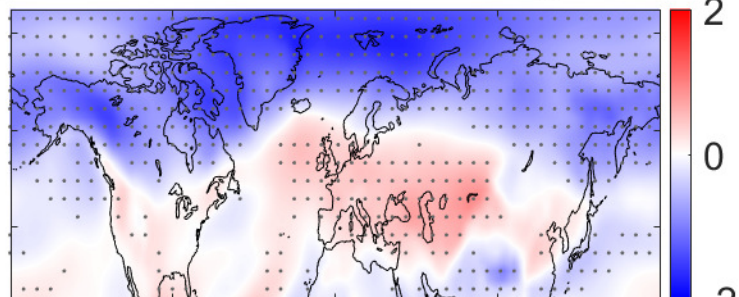
DJF

**b** Skewness estimated change

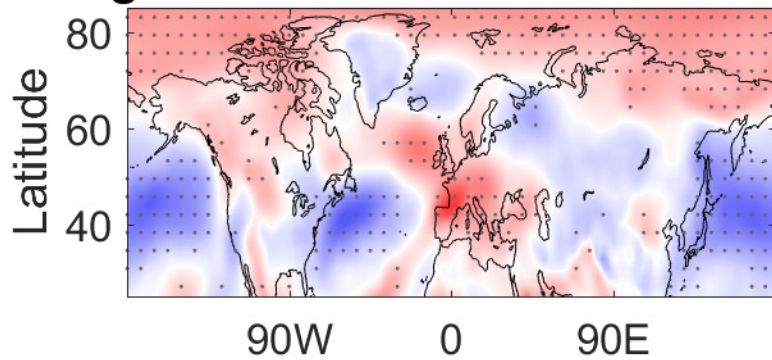
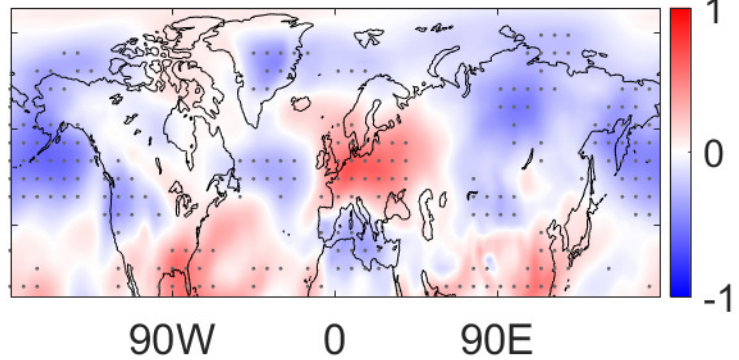
JJA

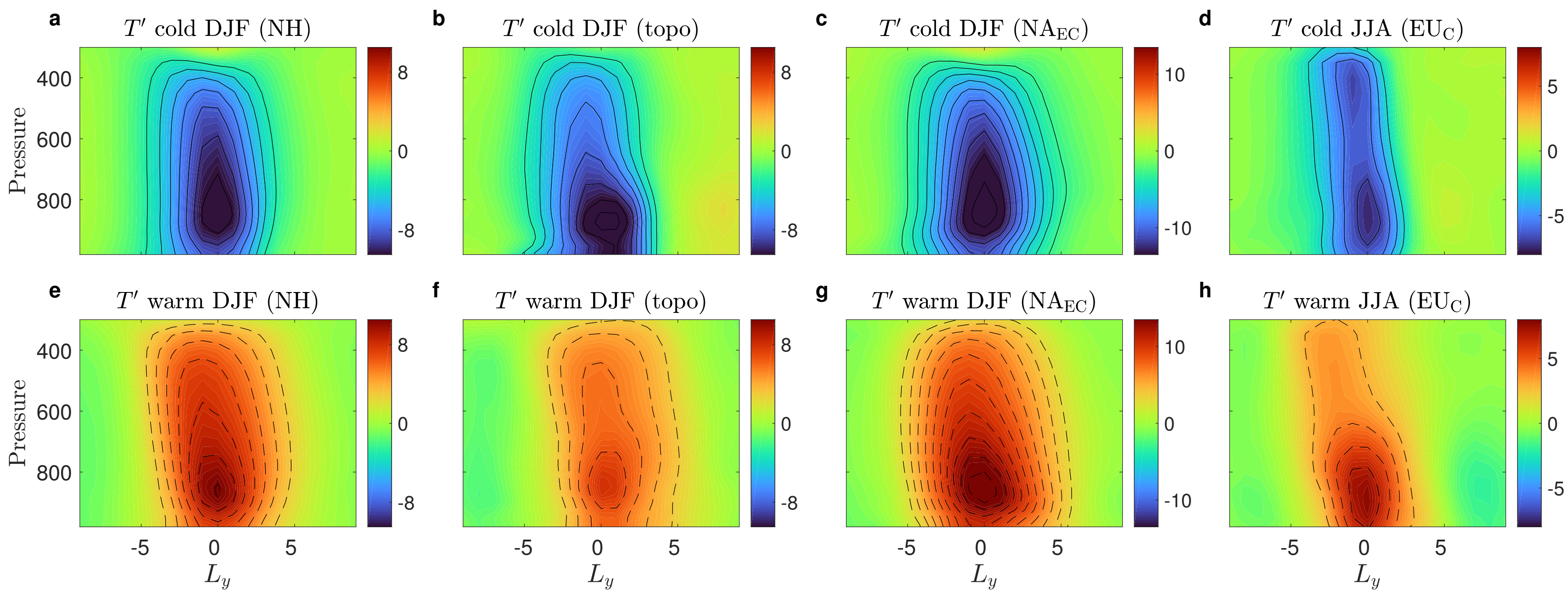
**e** Cold estimated change

DJF

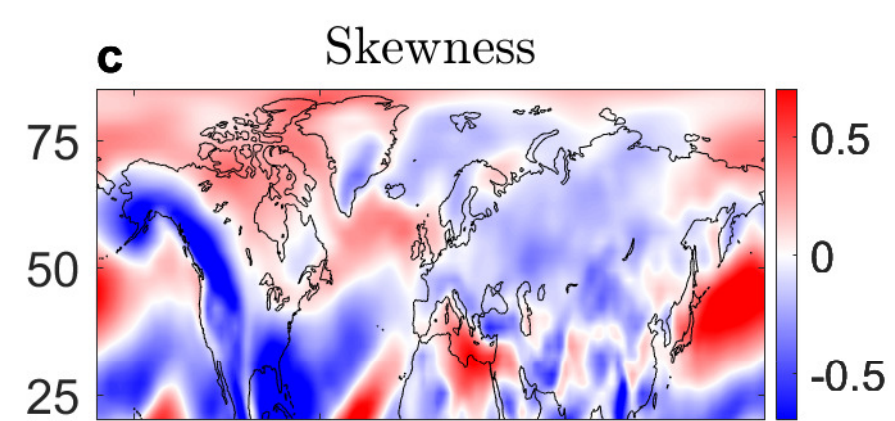
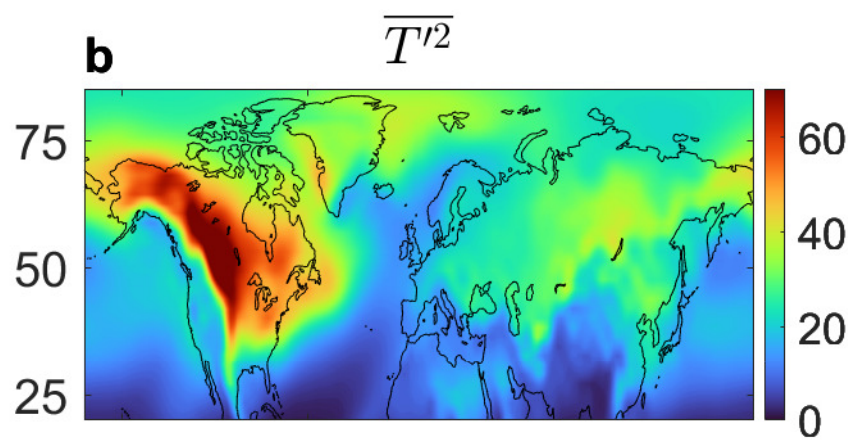
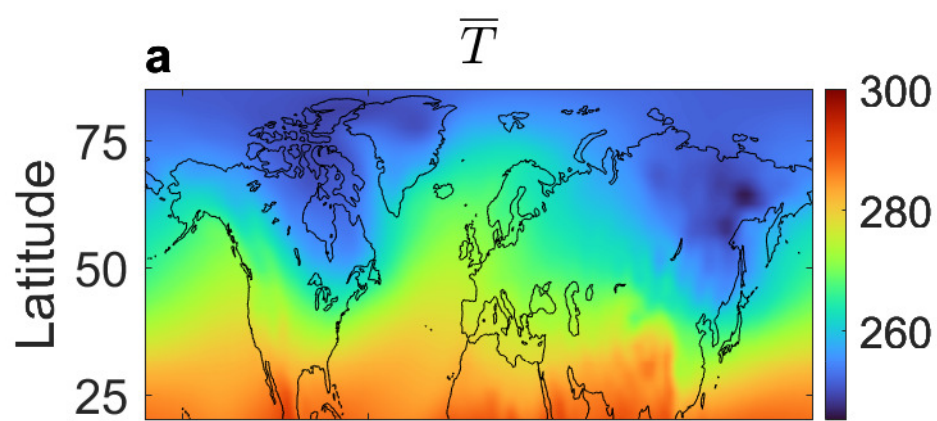
**f** Warm estimated change**g** Cold estimated change

JJA

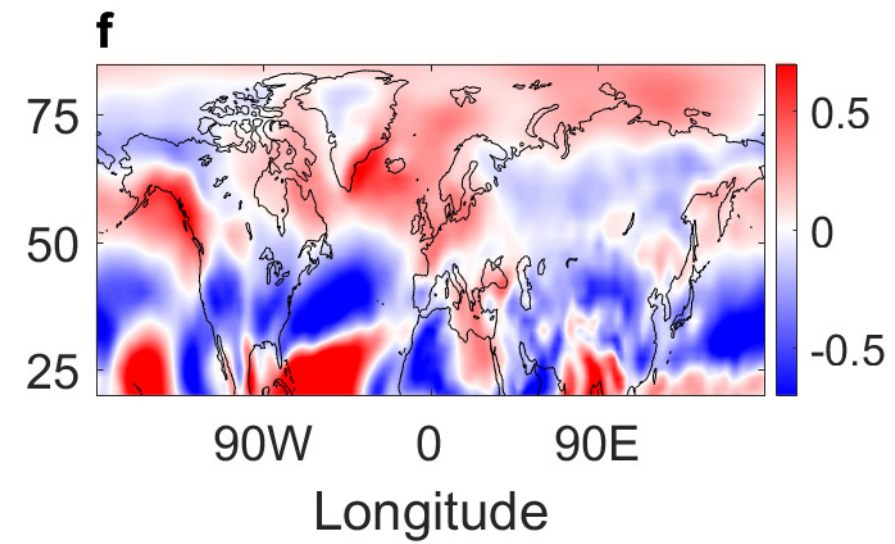
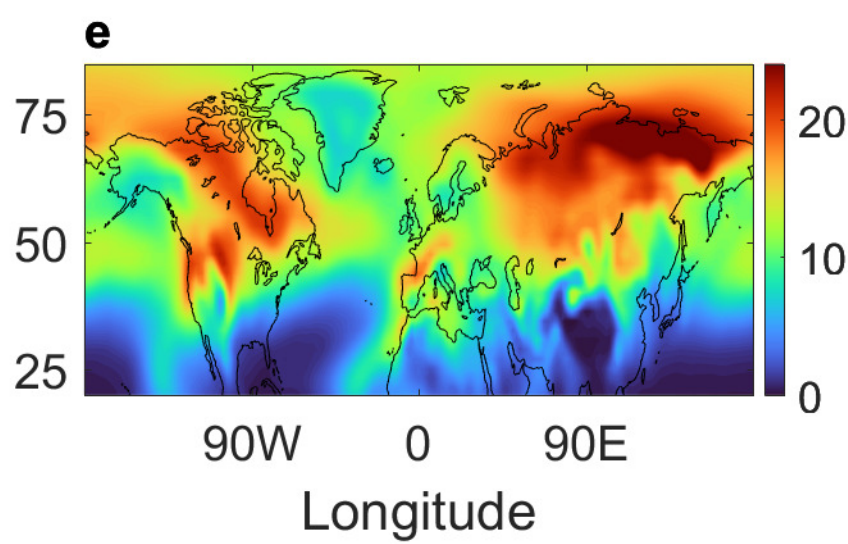
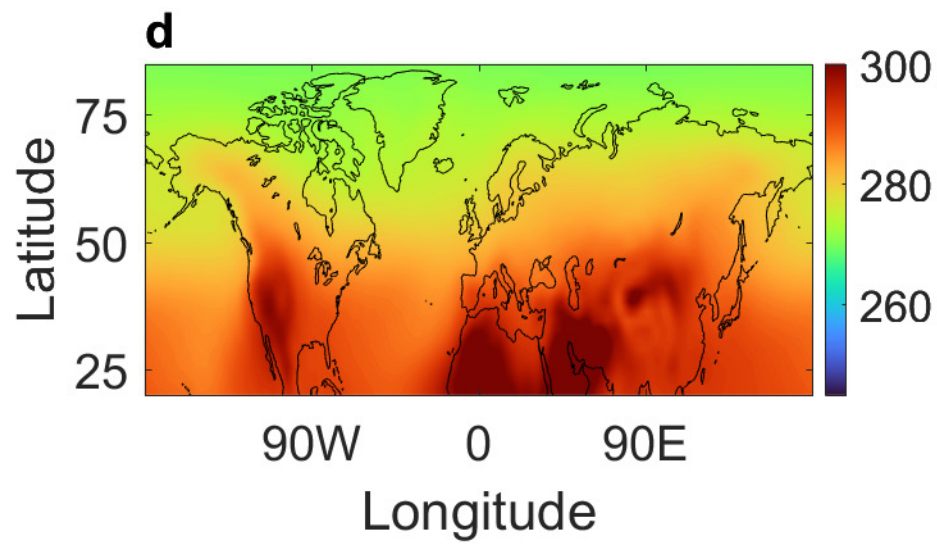
**h** Warm estimated change



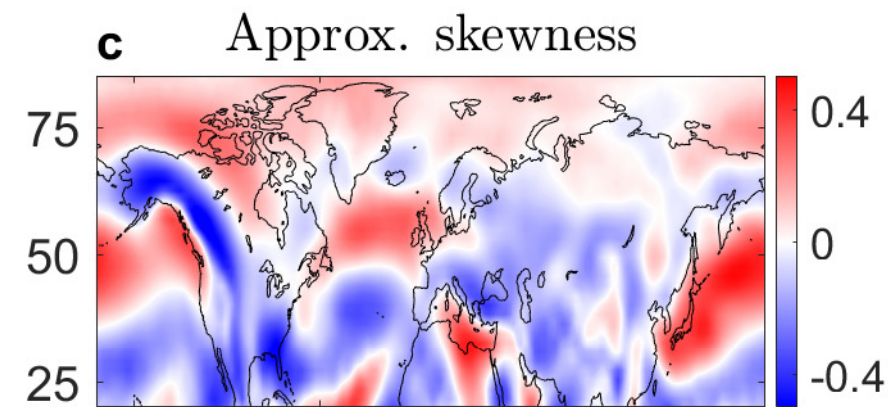
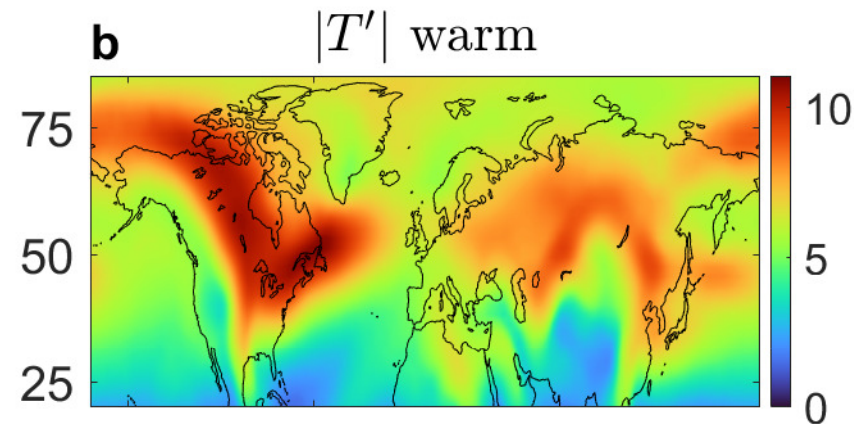
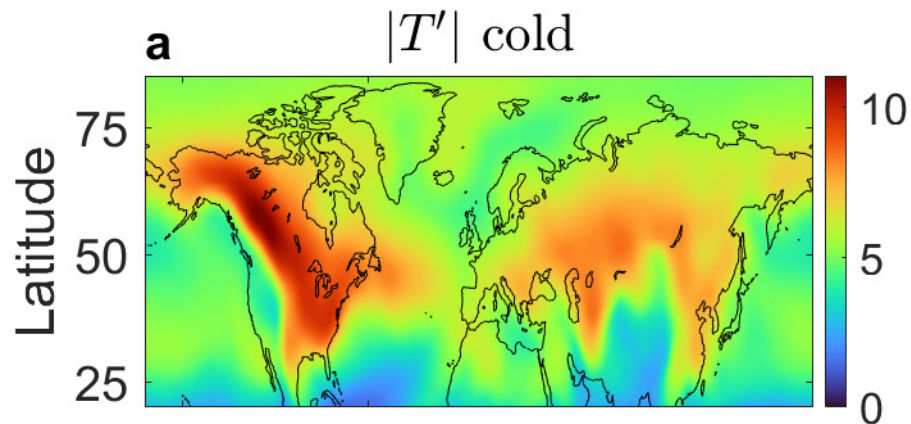
DJF



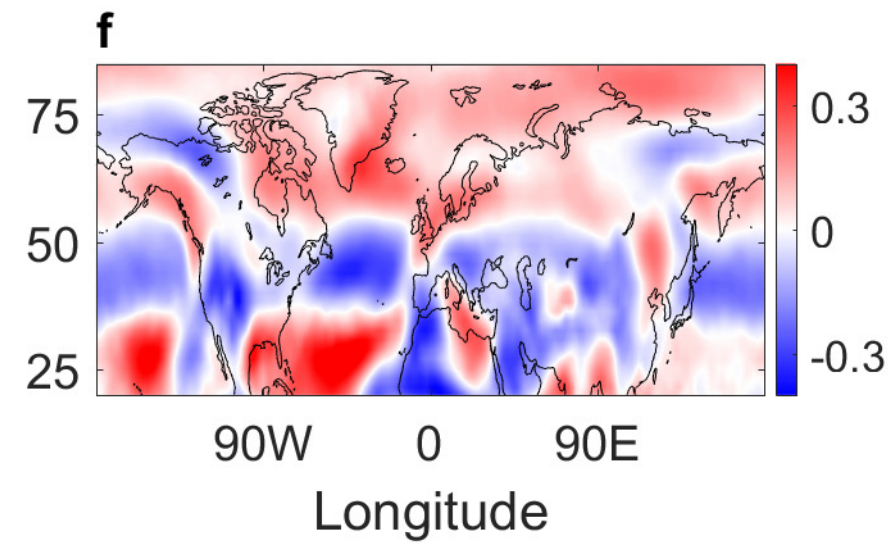
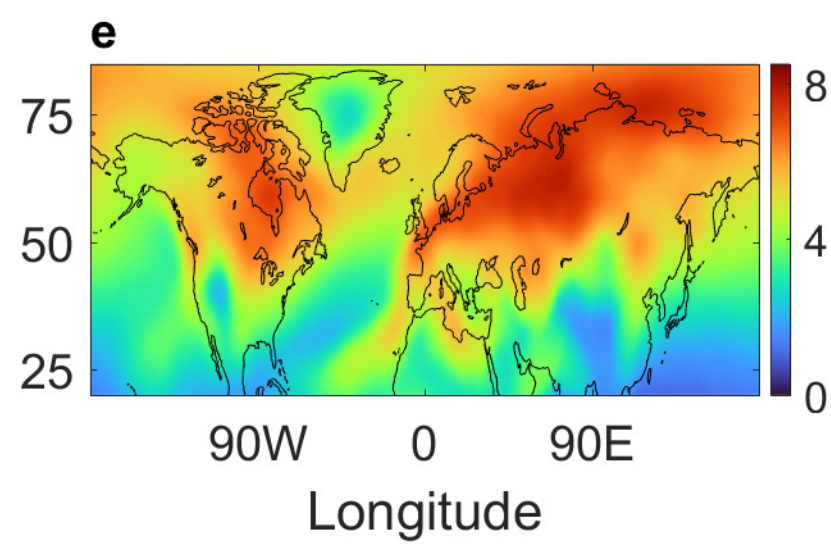
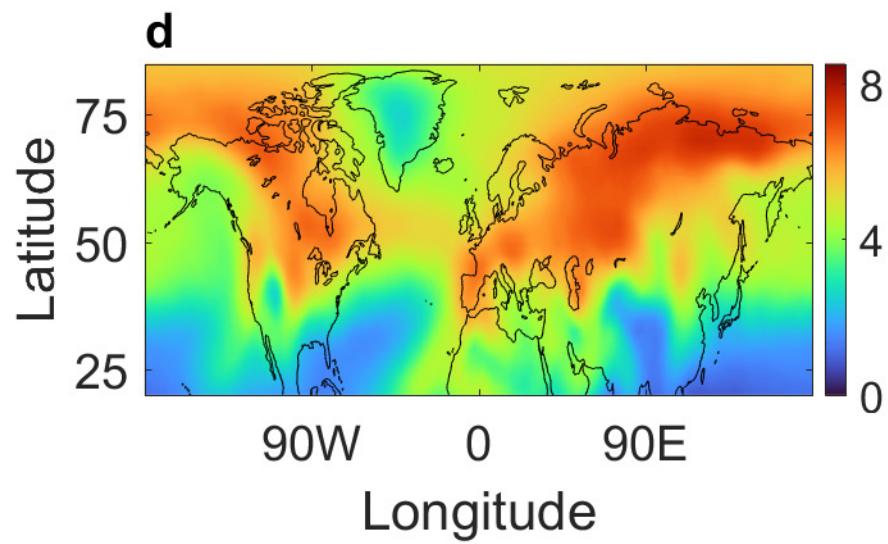
JJA



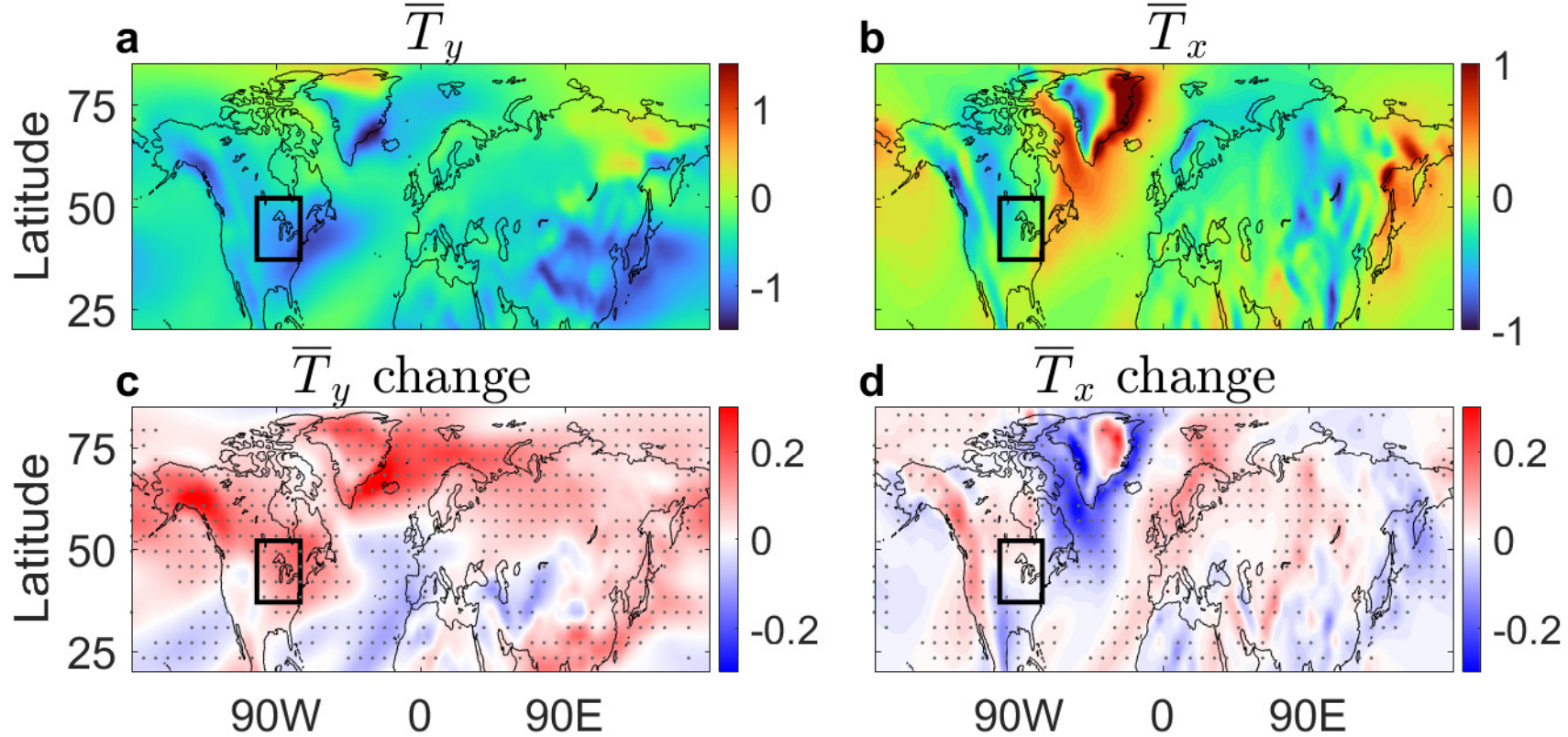
DJF



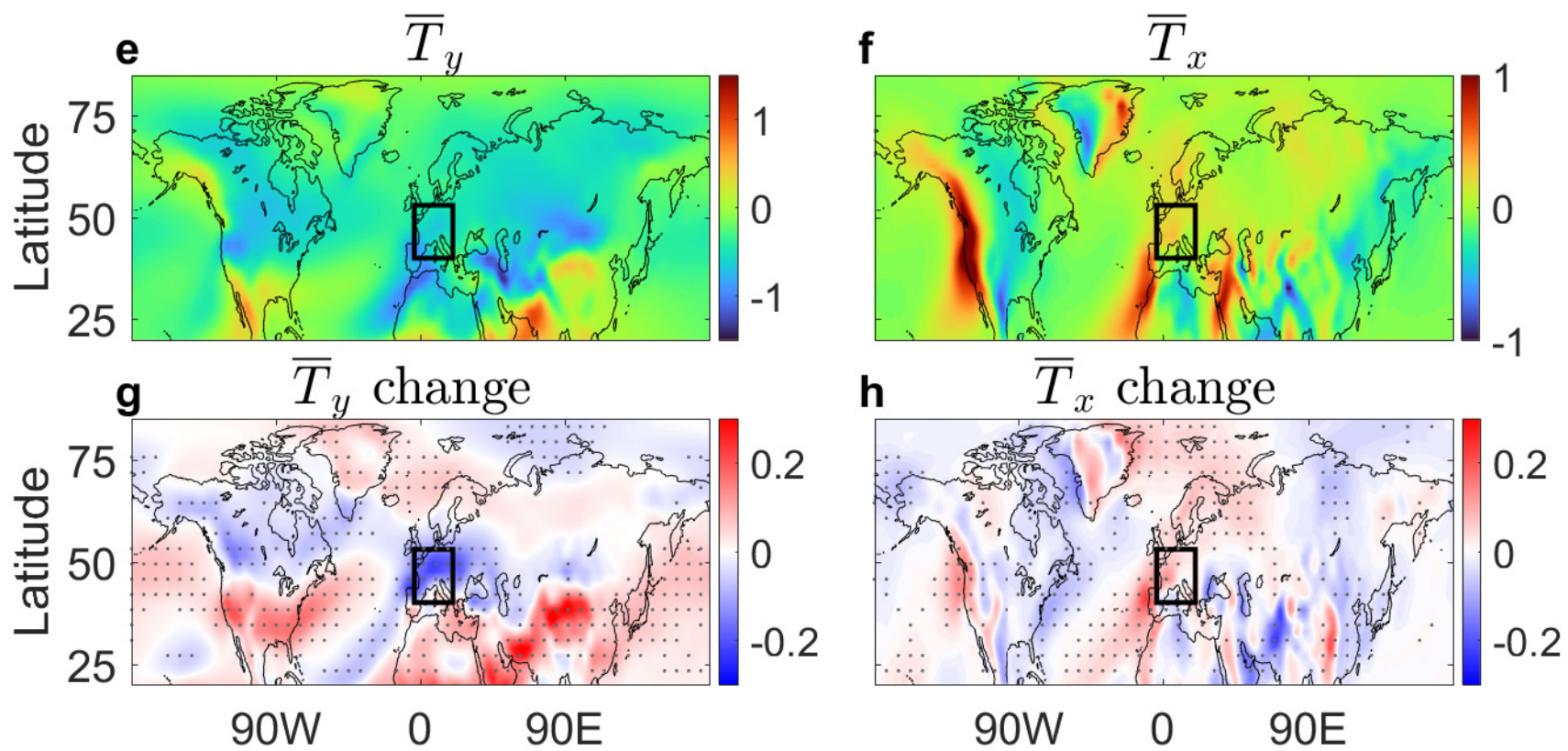
JJA



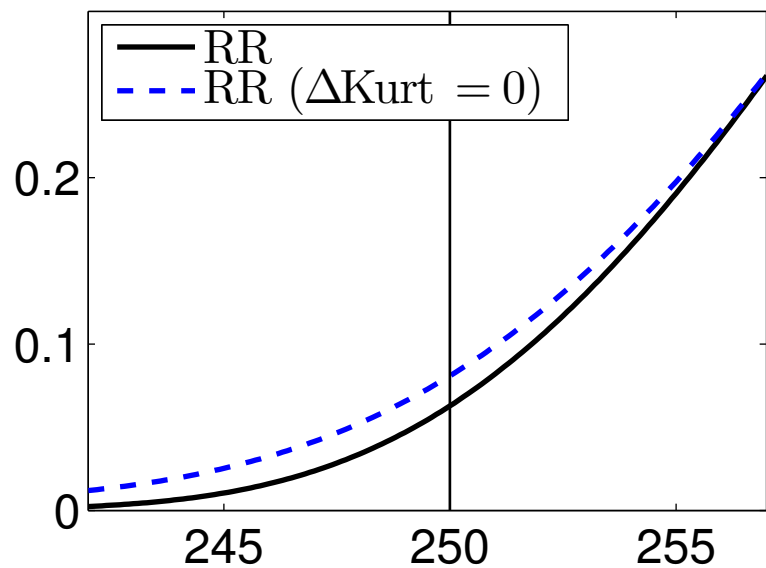
DJF



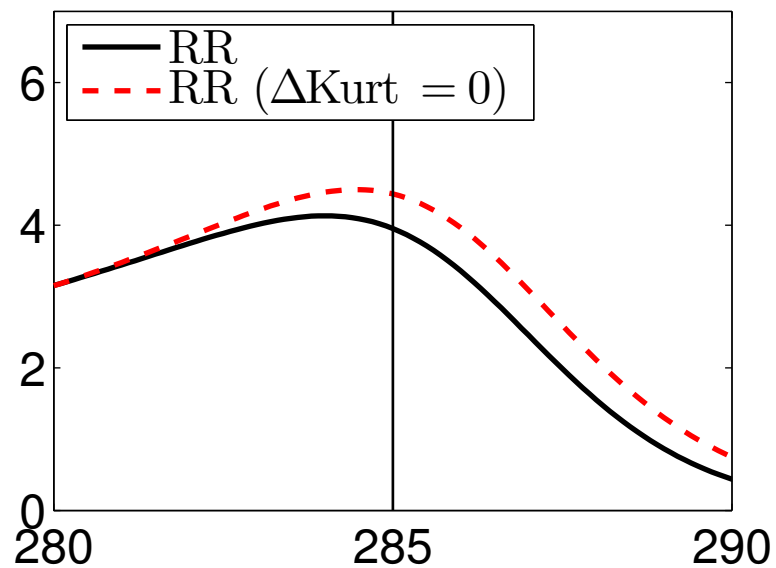
JJA



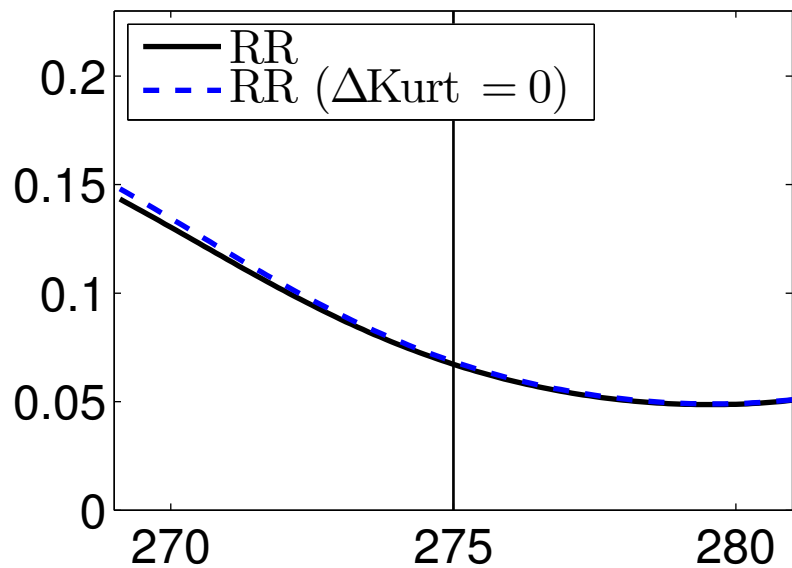
a Risk Ratio (NA_{EC} DJF) cold



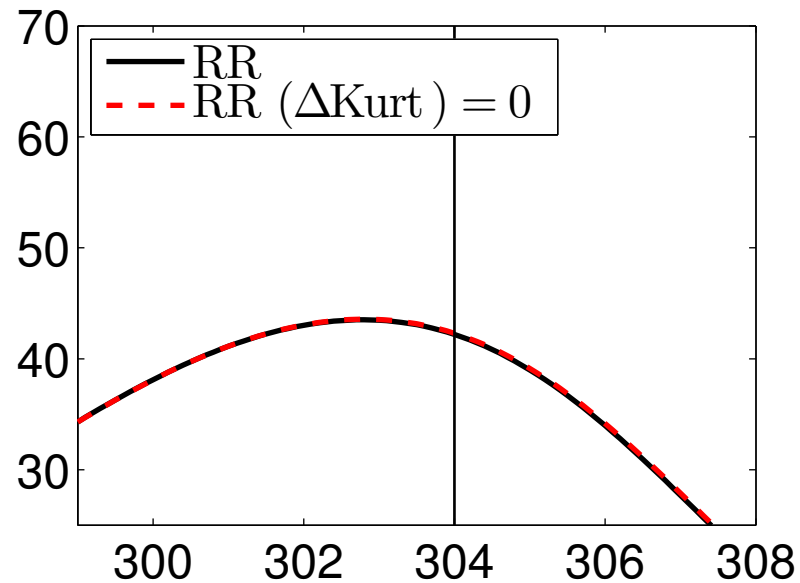
b Risk Ratio (NA_{EC} DJF) warm

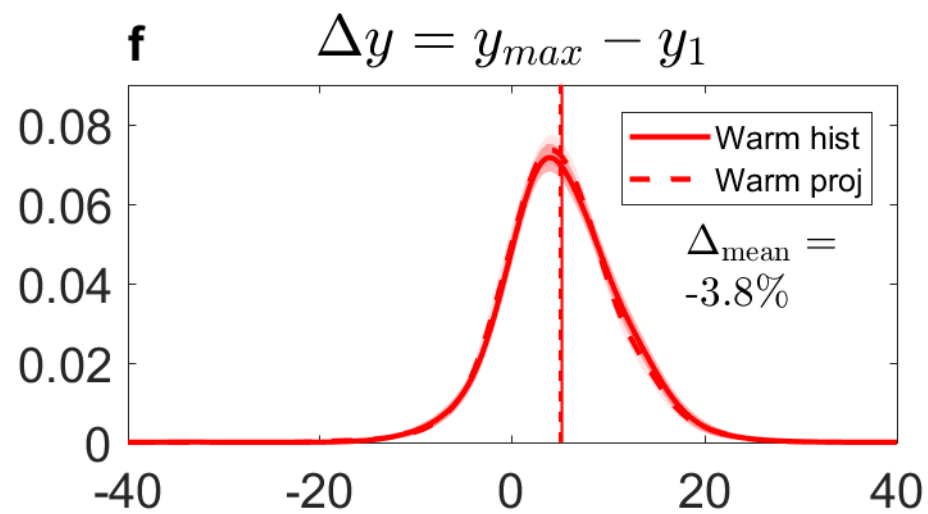
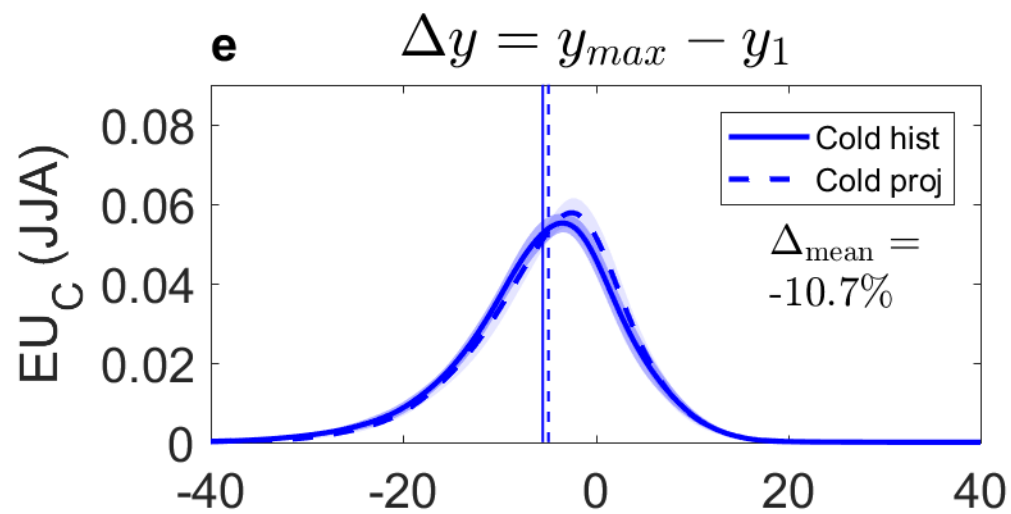
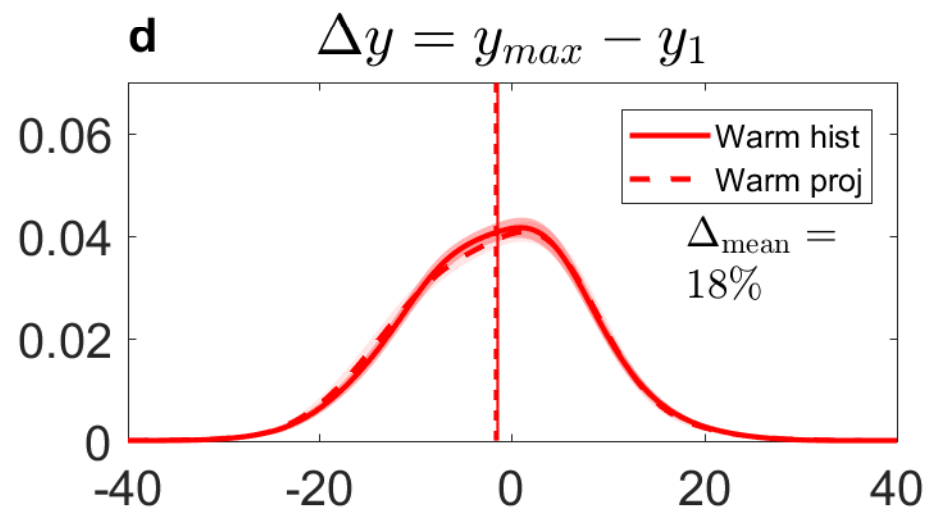
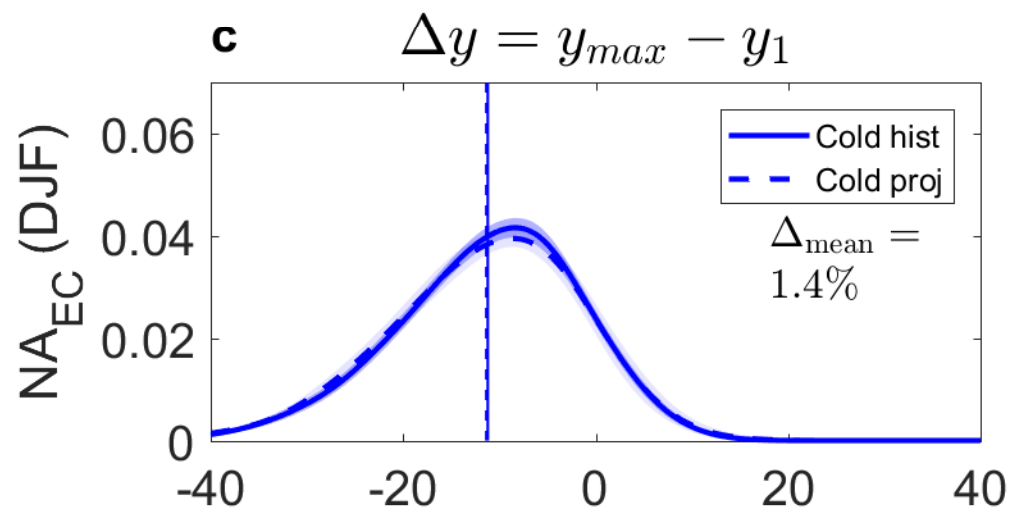
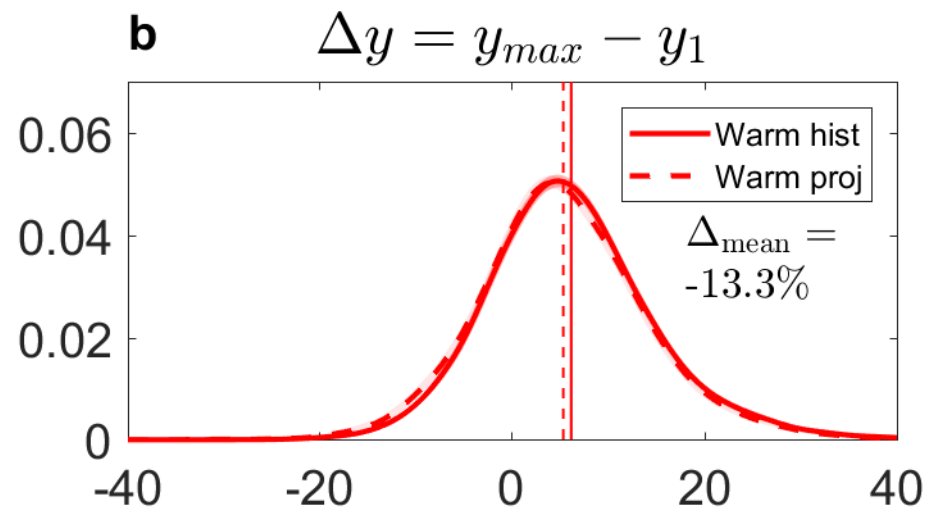
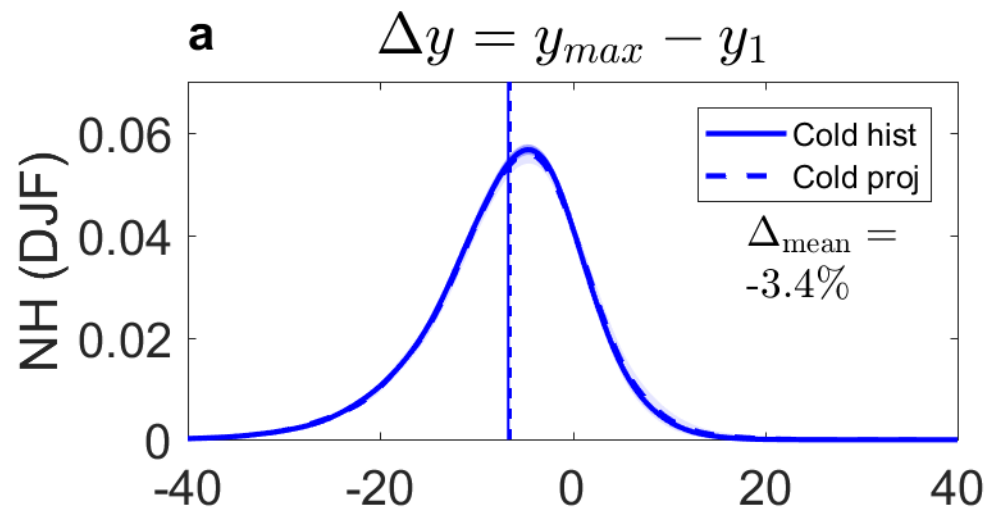


c Risk Ratio (E_C JJA) cold

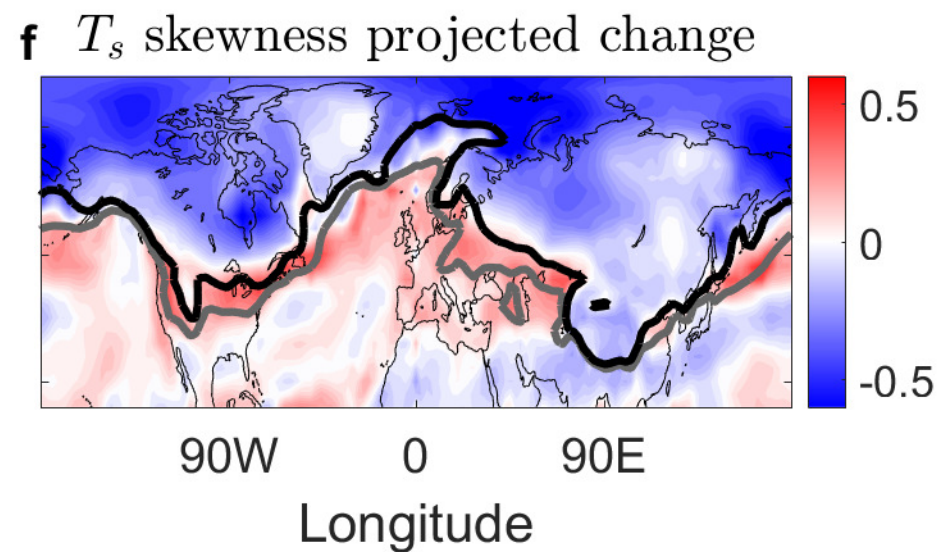
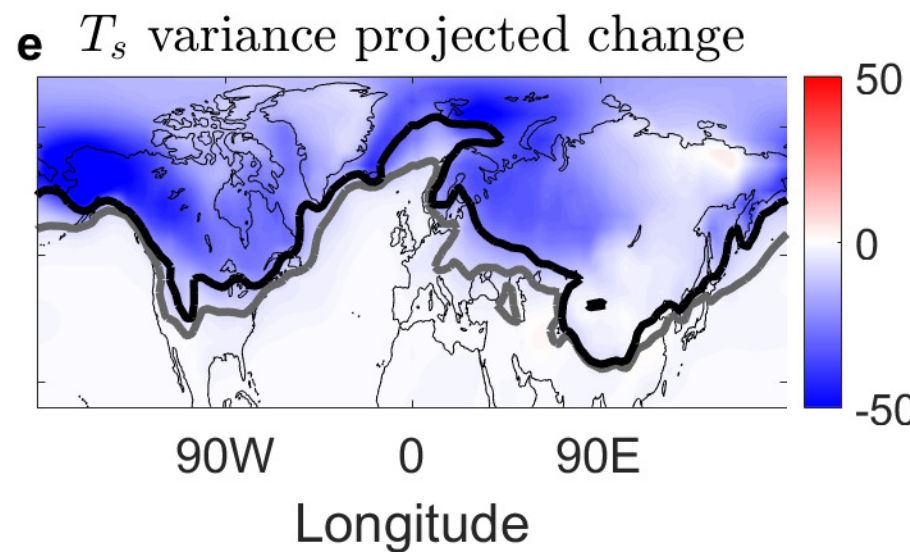
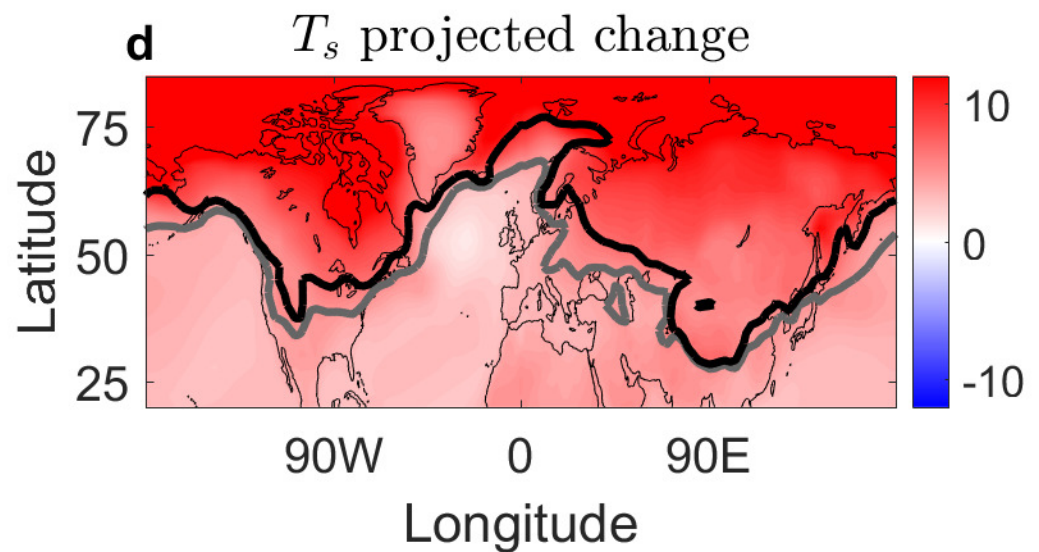
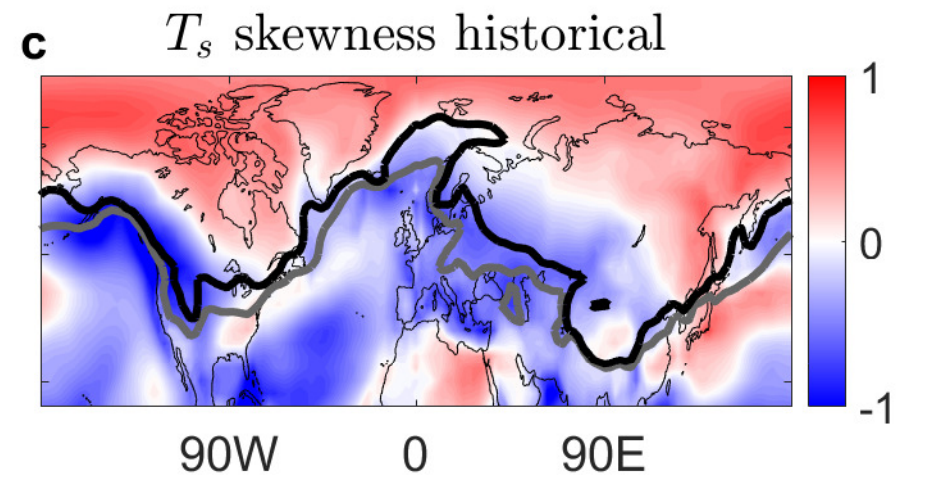
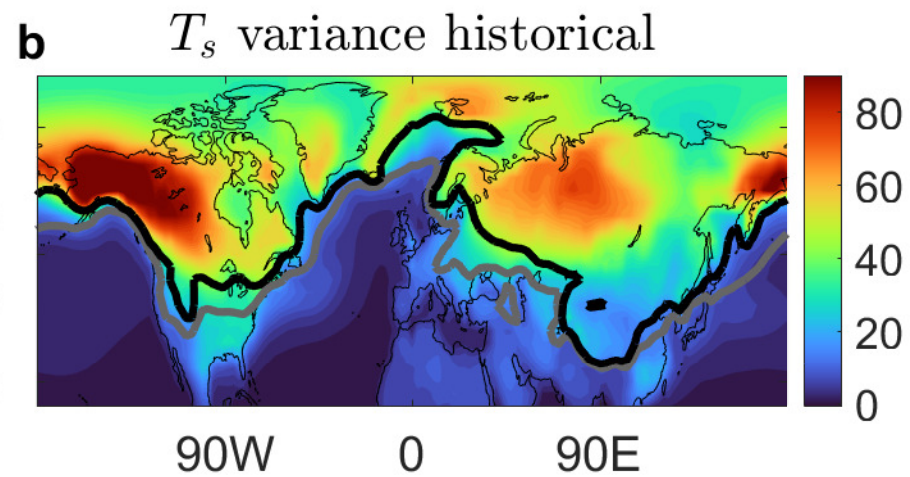
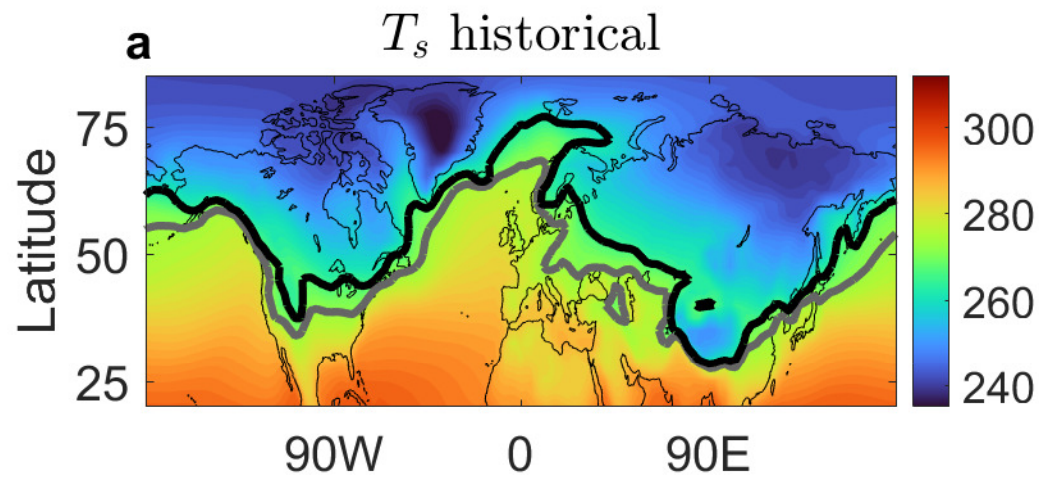


d Risk Ratio (E_C JJA) warm





DJF



JJA